LIMNOLOGY and OCEANOGRAPHY

ASLO

Limnol. Oceanogr. 63, 2018, 2337–2358

doi: 10.1002/lno.10941

Turbulence in a small arctic pond

Sally MacIntyre,[1,2,3]* Adam. T. Crowe,[3] Alicia Cortés ,[2] Lars Arneborg[4]

[1]Department of Ecology, Evolution and Marine Biology, University of California, Santa Barbara, California
[2]Marine Science Institute, University of California, Santa Barbara, California
[3]Earth Research Institute, University of California, Santa Barbara, California
[4]Swedish Meteorological and Hydrological Institute, Vastra Frolunda, Sweden

Abstract

Small ponds, numerous throughout the Arctic, are often supersaturated with climate-forcing trace gases. Improving estimates of emissions requires quantifying (1) their mixing dynamics and (2) near-surface turbulence which would enable emissions. To this end, we instrumented an arctic pond (510 m^2, 1 m deep) with a meteorological station, a thermistor array, and a vertically oriented acoustic Doppler velocimeter. We contrasted measured turbulence, as the rate of dissipation of turbulent kinetic energy, ε, with values predicted from Monin–Obukhov similarity theory (MOST) based on wind shear as u_{*w}, the water friction velocity, and buoyancy flux, β, under cooling. Stratification varied over diel cycles; the thermocline upwelled as winds changed allowing ventilation of near-bottom water. Near-surface temperature stratification was up to 7°C per meter. With respect to predictions from MOST: (1) With positive β under heating and strong near-surface stratification, turbulence was suppressed; (2) under heating with moderate stratification and under cooling with light to moderate winds, measured ε was in agreement with MOST; (3) under cooling with no wind and when surface currents had ceased, as occurred 20% of the time, turbulence was measurable and predicted from β. Near-surface turbulence was enhanced under cooling and light winds relative to that under a neutral atmosphere due to higher values of drag coefficients under unstable atmospheres. Small ponds are dynamic systems with wind-induced thermocline tilting enabling vertical exchanges. Near-surface turbulence, similar to that in larger systems, can be computed from surface meteorology enabling accurate estimates of gas transfer coefficients and emissions.

Ponds are ubiquitous on the landscape (Downing et al. 2006; Verpoorter et al. 2014) and contribute to regional and global carbon cycles via sequestration and emissions of carbon (Downing 2009; Laurion et al. 2010). Despite comprising about 9% of the surface area of lakes and ponds globally, very small ponds (surface area < 0.001 km^2) are estimated to contribute 15% of the diffusive emissions of CO_2 and 40% of the diffusive emissions of CH_4 (Holgerson and Raymond 2016). Increased diffusive emissions are predicted under warming scenarios (Wik et al. 2016*a*; Yvon-Durocher et al. 2017). Thaw ponds, a dominant feature of arctic lowlands (Wang et al. 2012; Muster et al. 2013), are typically 1–4 m deep and can be stratified with respect to temperature and oxygen within tens of centimeters of the surface (Negandhi et al. 2014; Matveev et al. 2016). Concentrations of CO_2 and CH_4 are supersaturated in surface waters and can be orders of magnitude higher near the bottom. They have well developed microbial communities including methanotrophs and methanogens (Crevecoeur et al. 2015, 2016) and process DOC from terrestrial and algal sources (Roiha et al. 2016). Carbon budgets from northern water bodies, however, are based on infrequent sampling which does not take into account the diel and synoptic variability in mixing which can moderate emissions (Liu et al. 2016; Wik et al. 2016*b*).

Studies of the mixing dynamics of ponds are rare, yet the contribution of ponds to carbon cycles depends, in part, on the frequency of events which bring dissolved gases to the air–water interface and on the magnitude of near surface turbulence which enables fluxes across the air–water interface. Time series temperature and dissolved oxygen measurements in arctic ponds indicate considerable temporal variability in near surface temperatures in summer and partial mixing of the water column in spring and fall (Laurion et al. 2010; Deshpande et al. 2015). It is not known whether near surface stratification damps turbulence or how deep and intense the mixing is at night. Wedderburn numbers have been computed for three subarctic ponds and indicate that upwelling and internal wave driven mixing may occur in spring and

*Correspondence: sally@eri.ucsb.edu

fall (Deshpande et al. 2015). The frequency of such events is not known in other locations. Nocturnal mixing, gravity currents from differential cooling (Monismith et al. 1990) or horizontal convective circulations (Lei and Patterson 2005; Bednarz et al. 2009*a*), and upwelling and related internal wave motions could enhance metabolic activity by transporting oxygen downwards and by transporting methane from the lower water column to the methanotrophs which can be abundant in the upper water column (Crevecoeur et al. 2015). The vertical transport could increase diffusive emissions. The extent to which these processes occur, as well as the magnitude of near surface turbulence, is currently unknown but important for developing a mechanistic understanding of controls on metabolism and diffusive fluxes from ponds.

Turbulence in ponds and lakes can be measured using acoustic Doppler velocimetry and temperature-gradient microstructure profiling and can be predicted from equations that take into account wind shear, quantified as u_{*w}, the water friction velocity, and buoyancy flux β from heat loss or gain (Gålfalk et al. 2013; Tedford et al. 2014). The turbulence is quantified as the rate of dissipation of turbulent kinetic energy, ε. The equations, based on Monin–Obukhov similarity theory (MOST) and quantified, for example in the open ocean under convection by Lombardo and Gregg (1989), enable turbulence to be computed as a function of depth within near surface regions energized by wind and buoyancy. This region is also known as the actively mixing layer (Imberger 1985). Implicit in similarity scaling, and excluding conditions with surface wave breaking, is that, at a minimum, turbulence production near the air–water interface is dominated by shear. That is, above a depth equal to the Monin-Obukhov length scale, here defined with the friction velocity in the water and the buoyancy flux into the actively mixing layer, $L_{MO} = u_{*w}^3/0.4\beta$, shear dominates production. It follows then that convection would dominate in the case of zero wind. In short, similarity scaling enables predictions of turbulence from meteorological measurements when the water column is stably or unstably stratified.

The stability of the atmosphere will modify near surface turbulence in the water column. When the atmosphere is stable (unstable), momentum, heat, and vapor fluxes flux are reduced (enhanced) relative to a neutral atmosphere (Csanady 2001). The drag and mass transfer coefficients used to compute these fluxes decrease as a function of wind speed for stable atmospheres whereas they increase under an unstable one (Csanady 2001; MacIntyre et al. 2002). For the same wind speed, near surface turbulence is expected to be lower when the atmosphere is stable than when it is neutral and higher when it is unstable. As the effects of atmospheric stability are more pronounced at lower wind speeds, the degree to which ponds and lakes are sheltered will determine the sensitivity of near-surface turbulence to atmospheric stability.

Improving the accuracy of estimates of diffusive emissions from ponds and lakes requires systematic studies to determine the frequency and efficacy of hydrodynamic processes which bring dissolved gases to the air–water interface, to quantify near-surface turbulence and how it is moderated by atmospheric and within lake stratification, and to validate meteorologically based equations for near-surface turbulence. For example, once ε has been measured or computed, the gas transfer coefficient, k, can be calculated using the surface renewal model (Zappa et al. 2007; MacIntyre et al. 2010) enabling diffusive fluxes to be computed. Fluxes within the water column can be computed using the coefficient of eddy diffusivity, K_z, which also depends on ε (Osborn 1980). The applicability of the similarity scaling in Tedford et al. (2014) for studies of greenhouse gas emissions has been demonstrated by eddy covariance studies in boreal lakes in Heiskanen et al. (2014) and Mammarella et al. (2015). Given that it allows ε and critical transport coefficients to be computed from basic meteorological and temperature measurements, further assessment of its generality is required by studies which include turbulence measurements.

The goal of our study was to quantify thermal structure and turbulence within a small arctic pond under diel changes in meteorology. We quantified near surface turbulence during windy and calm periods using an acoustic Doppler velocimeter (ADV) and compared measured dissipation rates with those obtained using the similarity equations in Tedford et al. (2014). In addition to our goal of determining whether the algorithms for ε apply in small ponds, we addressed whether turbulence at low winds under cooling conditions was enhanced by the increases in momentum flux from an unstable atmosphere, whether turbulence was produced by convection when winds and currents ceased, and whether near surface turbulence was decreased during heating. We computed Lake numbers, whose interpretation is similar to that for Wedderburn numbers (MacIntyre et al. 1999), and verify their predictions of the extent of upwelling against our measurements of thermal structure. We quantify K_z over diel cycles by using a modification of Jassby and Powell (1975) at night and following Osborn (1980) with the Shih et al. (2005) and Bouffard and Boegman (2013) algorithms in the day. As will be seen, dissipation rates follow the similarity scaling and are similar to those in much larger water bodies under cooling but are damped under heating, Lake numbers indicate considerable tilting of the thermocline, and computed gas transfer coefficients are at least double those for a neutral atmosphere at low winds and are twice those obtained using a commonly used wind-based model once winds exceed 2 m s^{-1}.

Site description and methods

Toolik Small Pond (68.625828 N, 149.596687 W) lies in a sloping region adjacent to Toolik Inlet and Toolik Lake, Alaska (Fig. 1a). The pond's surface area is 510 m^2 and maximum depth is 1.1 m (Fig. 1b). The pond is in the size class of very small ponds (Holgerson and Raymond 2016). Ponds up to 1000 m^2 in surface area are minimally 60% of the number of water bodies in three low-lying arctic regions. The terrain to the north and south shores is steeper, 6.5%

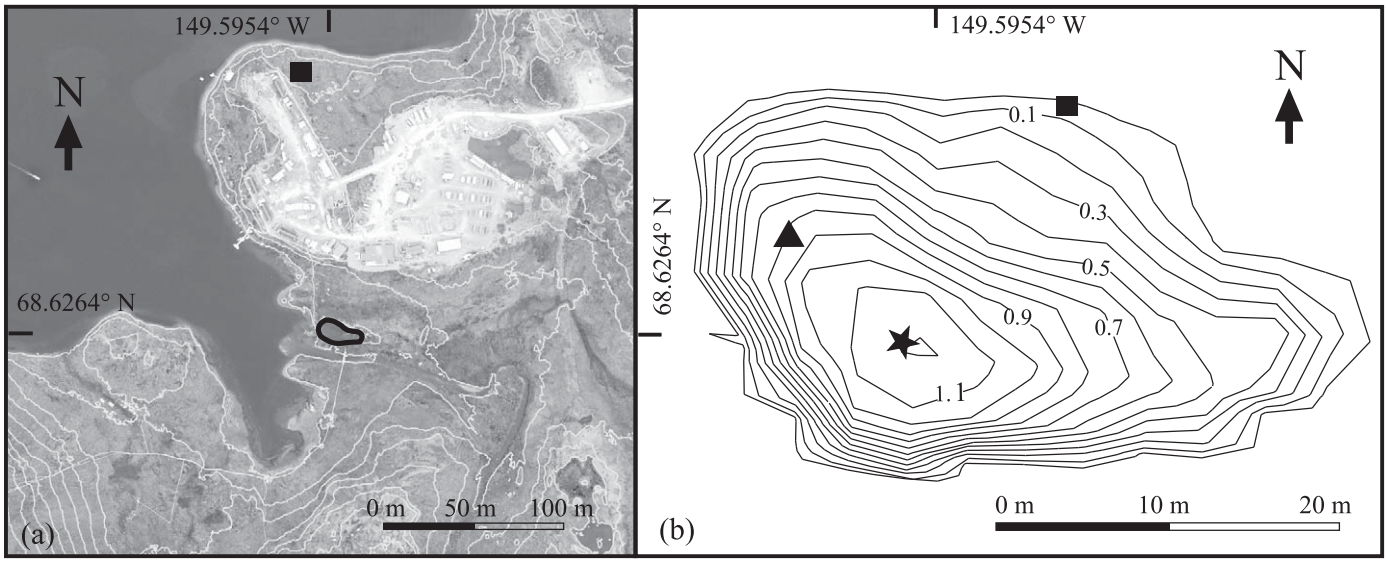

Fig. 1. (**a**) Map of region surrounding Toolik Small Pond, outlined in black, with Toolik Lake in the upper left and contours (2 m intervals, white) showing the topography surrounding the pond; (**b**) Bathymetric map of Toolik Small Pond with contours at 0.1 m intervals. Star marks the location of the ADV and triangle the position of the thermistor chain. Meteorological stations on land and adjacent to the pond are indicated by boxes in each panel. Due to failure of the wind vane at the exposed meteorological station located to the north of the pond, wind direction was obtained from an anemometer and wind vane at an exposed location 100 m to the northeast of the pond.

and 8%, respectively, than that to the east, 4%. Toolik Lake is to the west and was ice covered at the start of the study. Bottom slopes in Toolik Small Pond range from 0.05 to 0.1. Streams were not flowing into or out of the pond at the time of our study. Nearby vegetation is typical of tundra regions and includes *Eriophylum* species and occasional small willows.

The pond was instrumented from day 169 to day 178, 18 to 27 June, 2014. A meteorological station was mounted on a platform in the shallow nearshore region with instrumentation including a wind vane and anemometer, threshold 1.0 m s^{-1}, 2.2 m above the water surface and a shielded air temperature sensor, 0.2°C accuracy, and relative humidity sensor, 2.5% accuracy. Sensors were sampled every second and averaged over 5 min. Despite the manufacturers reported threshold for wind speed, the anemometer reported averages down to 0 m s^{-1}. The University of Alaska Toolik Field Station (UAF TFS) meteorological station adjacent to Toolik Lake and 250 m from the pond includes an R.M. Young anemometer 05103 and 05106 with instrument threshold 0.5 m s^{-1} and shielded Vaisala HMP 155A air temperature and relative humidity sensor with sampling regime as above. Downwelling long and shortwave radiation were measured with a Kipp and Zonen CNR 4 at the UAF TFS meteorological station. Rainfall was measured with a tipping bucket rain gauge. The thermistor array was deployed at a depth of 0.75 m and consisted of Onset Water Temp Pros deployed on a taut mooring with temperature loggers 0.01 m, 0.12 m, 0.25 m, 0.38 m, 0.5 m, and 0.75 m below the surface. Manufacturer reported temperature accuracy is 0.2°C and resolution 0.02°C. We post-calibrated the loggers in an insulated water bath at 5 temperatures from 8°C to 18°C. We used this data to adjust the offsets of the individual loggers and improved their accuracy to 0.04°C. The depth of the actively mixing layer was computed using a temperature difference relative to the surface of 0.04°C (Tedford et al. 2014). A Ricoh WG-4 waterproof camera was mounted adjacent to the pond and took photographs at 3-min intervals. We subsequently evaluated the presence or absence of surface waves and their prevalence on a scale of 0 to 3. Amplitude was always less than 10 cm. Morphometry was obtained over a measured grid using a marked sounding line. The resulting hypsographic curve was used to compute heat budgets for comparison with the surface energy budget and as needed to compute the attenuation of light and the coefficient of eddy diffusivity described below.

Acoustic doppler velocimetry

The three components of velocity were measured with a Nortek Vector ADV anchored at the bottom and maintained in a vertical orientation with buoyancy provided by Styrofoam floats in a collar just below the transducer arms. Sampling was at 32 Hz with each deployment lasting slightly longer than a day with duration dependent on instrument memory. Due to the multiple deployments required, the depth of the measurement volume ranged from 9 cm to 33 cm below the air–water interface. Detailed analyses were done when its depth was between 9 cm and 15 cm below the interface. Pitch and roll corrections were done using software provided by Nortek. Data were averaged in 5-min blocks.

Turbulence was quantified as the rate of dissipation of turbulent kinetic energy, ε, by fitting observed vertical velocity

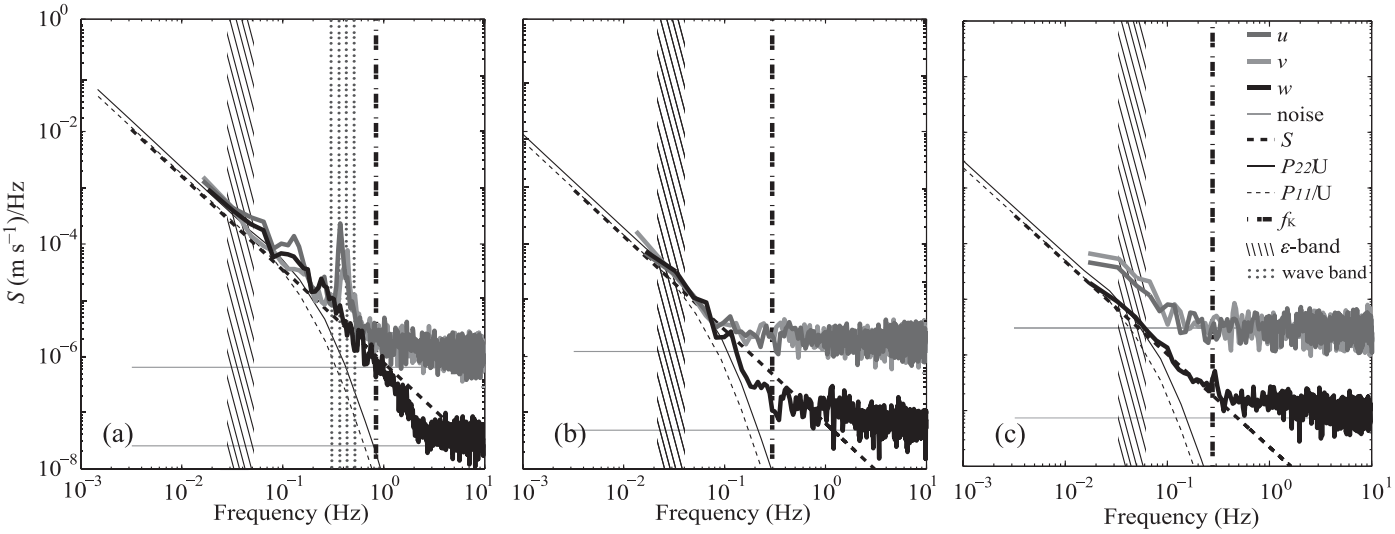

Fig. 2. Power spectral density per unit frequency for the three ADV velocity components (longitudinal *u*, transversal *v*, and vertical *w*) for three selected 5-min intervals. Spectra decay with a −5/3 slope. Region of the spectrum used to estimate rate of dissipation of turbulent kinetic energy (ε-band, diagonal lines), frequency band for surface waves (dotted region): (**a**) surface waves are present, and the three velocity components overlap in the ε-band indicating homogeneous, isotropic turbulence; (**b**) surface waves were not present and the three spectra overlap in the ε-band indicating homogeneous, isotropic turbulence; (**c**) the horizontal velocity spectra are nearly an order of magnitude higher than the vertical in the ε-band indicating conditions are not met for homogeneous, isotropic turbulence. Key to details: −5/3 slope (dashed line), energy level of noise for horizontal velocities (upper light gray horizontal line) and for vertical velocity (lower light gray horizontal line), Kolmogorov frequency (f_k) where $f_k = k_K$*U and $k_K = (\varepsilon/\upsilon^3)^{0.25}/2\pi$) (dashed-dot vertical line), Nasmyth spectra P_{22}/U and P_{11}/U as across-flow and along-flow components, respectively (darker and lighter gray curves) with fitting done with the P_{22}/U curve.

spectra to the universal Nasmyth spectra (Oakey 1982). Transformation from frequency space to wave number space is possible when currents are large enough that the assumptions of Taylor's hypothesis are met, that is, that the turbulent velocity fluctuations are much smaller than the mean flow (Tennekes and Lumley 1972). This approach is also known as the frozen-turbulence approximation. To avoid the confounding influence of surface waves, the fitting to the Nasmyth spectrum was done in the low wave number/low frequency portion of the power spectrum (Fig. 2a,b). Despite the low flows, the turbulence was often sufficiently high that the inertial subrange existed as evidenced by the spectra decreasing with a −5/3 slope relative to wavenumber. P_{11}/U and P_{22}/U show the Nasmyth spectra (Oakey 1982) in frequency space (Fig. 2), with P_{11} the along-flow component and P_{22} the across flow component. The dissipation rate is found by fitting the vertical velocity spectrum to the upper of these curves, P_{22}/U, since the vertical velocity is perpendicular to the mean (horizontal) flow. The confidence levels of each spectral point were estimated using an assumption of a chi-squared distribution of the spectral averaging. In our case with ∼ 2000 data points and half overlapping windows, the 95% confidence limits are 0.6 and 2.2 times the spectral value. These limits do not represent the uncertainty in the analysis. For example, each dissipation rate estimate is based on 2–5 spectral points so the limits are somewhat less. Were each dissipation rate estimate based on 5 spectral points, the degrees of freedom in the spectral averaging would increase resulting in a correspondingly narrower confidence interval (about 0.77 to 1.33 times the spectral mean value). That said, confidence intervals are generally used to determine the significance of peaks in spectra. As is typical with acoustic Doppler velocimetry, the goal is to illustrate that the spectra fall off with a −5/3 slope and the validation is done graphically as here (Voulgaris and Trowbridge 1998; Davis and Monismith 2011).

Computing dissipation using the universal turbulence spectra assumes that the turbulence is homogeneous and isotropic and that an inertial subrange exists (Tennekes and Lumley 1972; Thorpe 2007). Spectra for the *u* and *v* components and *w* velocities were often of similar magnitude and decayed following the −5/3 law expected within the inertial subrange when turbulence is homogeneous and isotropic with or without surface waves (Fig. 2a,b). Under these conditions, we accepted the computed ε. At frequencies higher than that of the surface waves, spectra for the *u* and *v* components were flat and due to noise whereas the spectra rolled off rapidly for the *w* component in accordance with the Nasmyth spectrum. At other times, spectra for the three velocity components decayed with a −5/3 slope at low frequencies but the *u* and *v* components were more energetic than the *w* component, at times by more than an order of magnitude (Fig. 2c). The differences in the magnitude of the spectra indicate that the turbulence was anisotropic and thus ε could not be computed assuming an inertial subrange. We accepted data if the spectra decayed with a negative

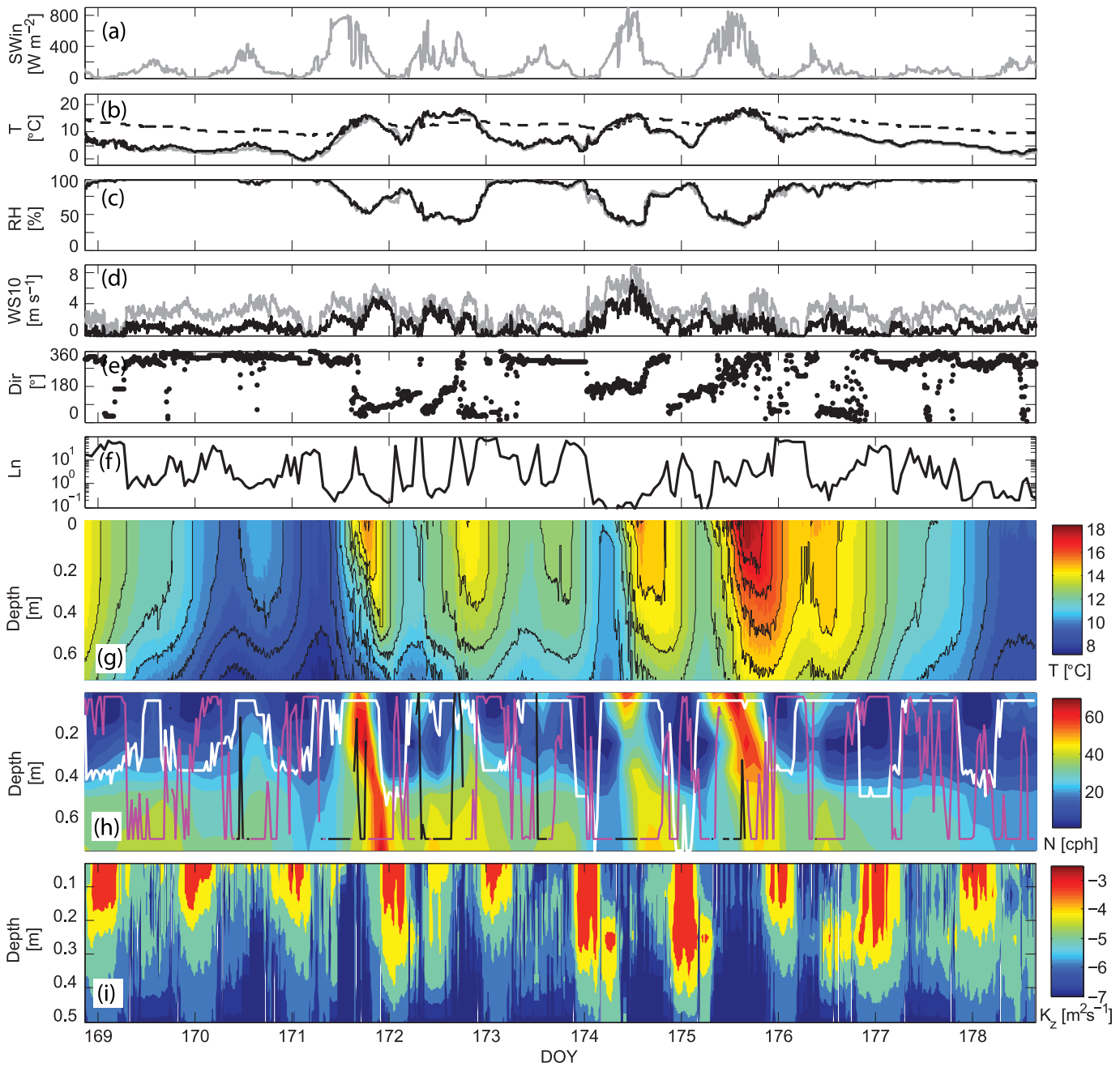

Fig. 3. Time series meteorological data in June 2014 obtained adjacent to the pond (black) and at a land station 250 m away (gray) and concurrent conditions within the pond. (**a**) Incoming shortwave radiation from the land station, SW_{in}; (**b**) surface water (--) and air temperatures (-), T; (**c**) relative humidity, RH; (**d**) wind speed normalized to 10 m following law of the wall scaling for neutral boundary layers, WS10; (**e**) wind direction, Dir; (**f**) Lake number, L_N; (**g**) water temperatures, T; (**h**) buoyancy frequency N with depth of the actively mixing layer, z_{AML}, defined by a temperature difference of 0.04°C (white), Monin–Obukhov length scale, L_{MO}, under cooling (magenta) and under heating (black) with maximum and minimum values scaled to fit in the figure. z_{AML} extends to the surface at midday but drawn as 0.06 m as it is operationally defined as intermediate in depth between the upper two loggers; (i) coefficient of eddy diffusivity in logarithmic scale, K_z (note change in scale of y-axis in this panel).

slope for all three components and computed dissipation from the w spectra were no more than three times less than computed from the u and v spectra. This value takes into account the confidence intervals of the measurements. We also used a cutoff of 2, and the only appreciable change in results in the analysis was to lose three data points during heating with light winds. The fourth condition observed (not shown) was one in which the vertical velocity spectrum followed the −5/3 slope at low frequencies but the horizontal spectra were flat and equal in magnitude to the noise.

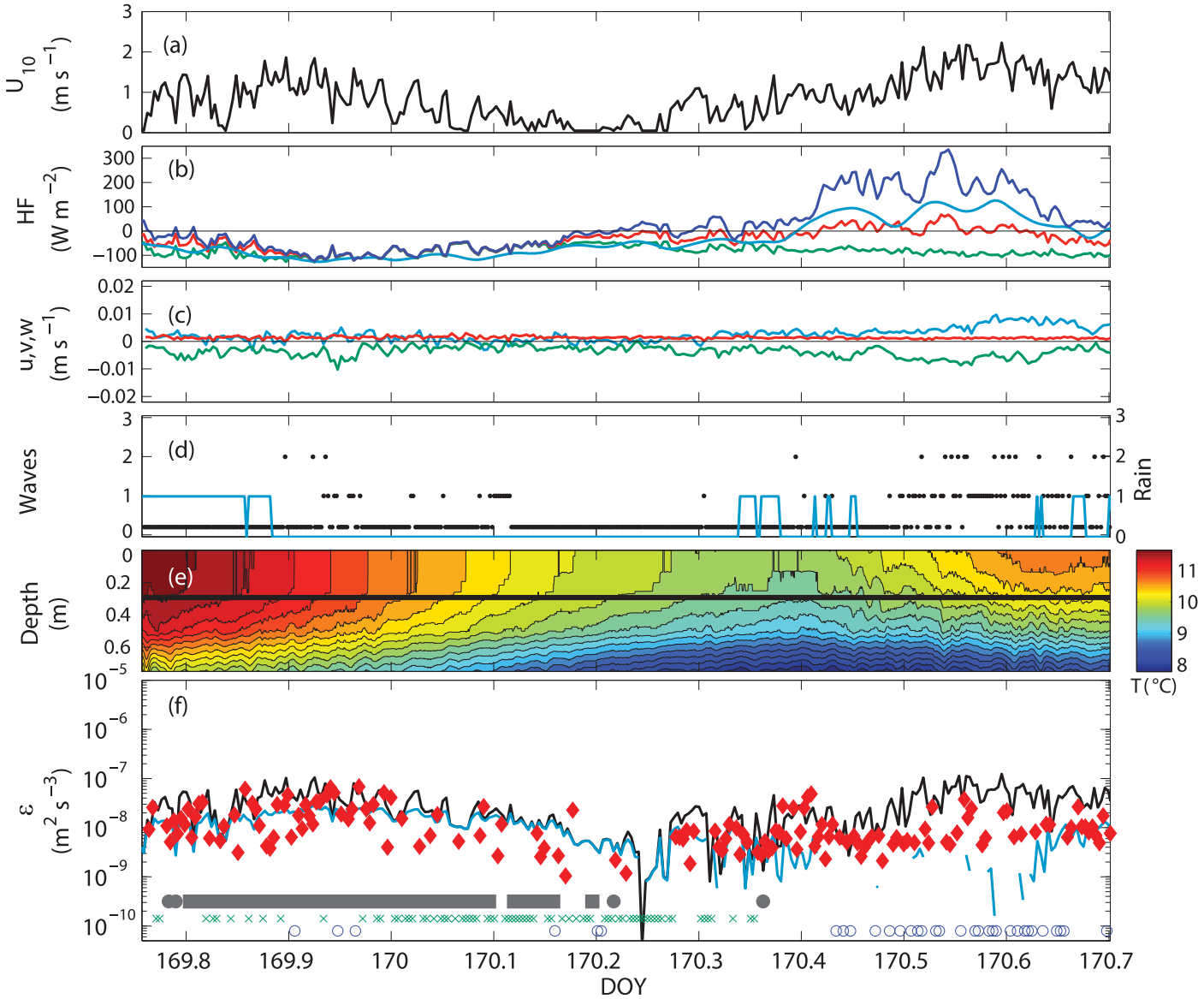

Fig. 4. Time series of (**a**) wind speed corrected to 10 m height, U_{10}; (**b**) Heat fluxes, HF: net surface fluxes computed as sum of latent and sensible heat fluxes and net long wave radiation (green), effective heat flux computed as in Imberger (1985) within the actively mixing layer (red), total heat flux computed as net short wave minus the surface heat fluxes (dark blue) and heat flux computed from change in heat content within the pond (light blue); (**c**) east (u, blue), north (v, green) and vertical (w, red) velocities measured by the ADV; (**d**) wave magnitude (black dots) based on photographs taken on the shore of the pond and evaluated as no waves (0) to surface filled with waves (3) and presence or absence of rain as light mist (blue); (**e**) temperatures, T, with isotherms overlaid and horizontal black line the depth of the measurement volume of the ADV, z_{ADV}, (**f**) time series of dissipation rates, ε, from ADV (red diamonds, spectra collapse as expected for homogeneous isotropic turbulence), from similarity scaling (black line) and from similarity scaling but only for buoyancy flux, β (blue line). That is, ε from buoyancy flux only is 0.77β. ADV within the actively mixing layer is indicated by horizontal gray bar. Cases in which Taylor's frozen field hypothesis were not met (green x's) and when criteria for homogeneous, isotropic turbulence were not met (blue circles).

Values of ε were accepted in that case. We computed the fraction of the time in each 5-min block when more than 10% and when more than 50% of the data had correlations less than 70%. Evaluation of spectra under those conditions indicated decay followed the $-5/3$ law even when up to 50% of the data had low correlations. These data were retained for the analysis.

Further calculations

The surface energy budget was calculated using bulk coefficients adjusted for atmospheric stability as in MacIntyre et al. (2002, 2014). Momentum and latent and sensible heat fluxes computed with these procedures differ by at most 10% from results obtained using COARE equations (Fairall et al. 1996; Tedford et al. 2014). When wind speeds dropped

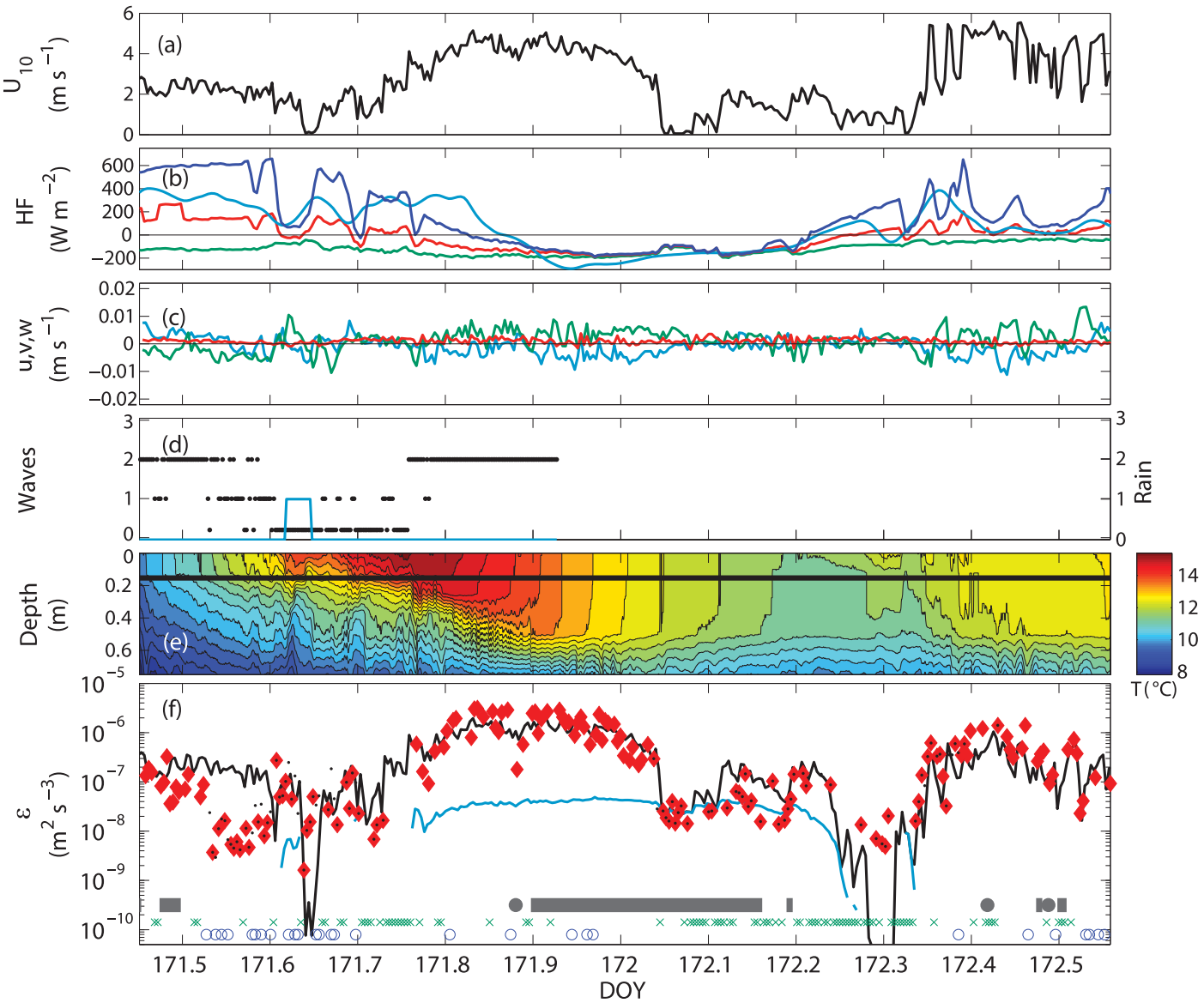

Fig. 5. As for Fig. 4 for days 171.4–172.55. Lower panel, black dots in center of diamonds indicate samples for which correlations for the ADV data were less than 70% in the *u*, *v*, or *w* directions more than 50% of the time. Spectra met our other criteria for acceptability (see methods), hence we include these results.

to 0 m s^{-1}, we assumed wind speeds were 0.1 m s^{-1}. These low values occurred near midnight and winds were northerly or easterly; winds similarly decreased around midnight 80% of the time at the exposed site (Fig. 3d,e). The computed latent and sensible heat fluxes for winds of 0.1 m s^{-1} were reasonable as values differed by at most 5–10 W m^{-2} from those computed for cases of no wind following Adams et al. (1990). We computed albedo taking into account zenith angle and angle of refraction, and calculated upwelling long wave radiation from surface water temperature using the Stefan–Boltzman equation (MacIntyre et al. 2002). At night, total heat flux into the lake computed from the surface meteorology, that is, the sum of net shortwave, latent and sensible heat fluxes, and net long wave radiation, was similar to the heat budget computed from time series temperature data (Figs. 4–8). The agreement indicates accuracy in the coefficients for mass transfer used to calculate sensible and latent heat fluxes and in the calculated outgoing long wave radiation. To obtain light attenuation, we compared measured changes in heat content in the pond against calculated changes in heat content to 75 cm using diffuse attenuation coefficients of 0.6 m^{-1} which is similar to values in nearby lakes, 1 m^{-1}, 1.7 m^{-1} and obtained the best match during heating across all days using $k_d = 1$ m^{-1}. Density of water, ρ_w, was computed following Chen and Millero (1977) with similar results obtained using more recent algorithms

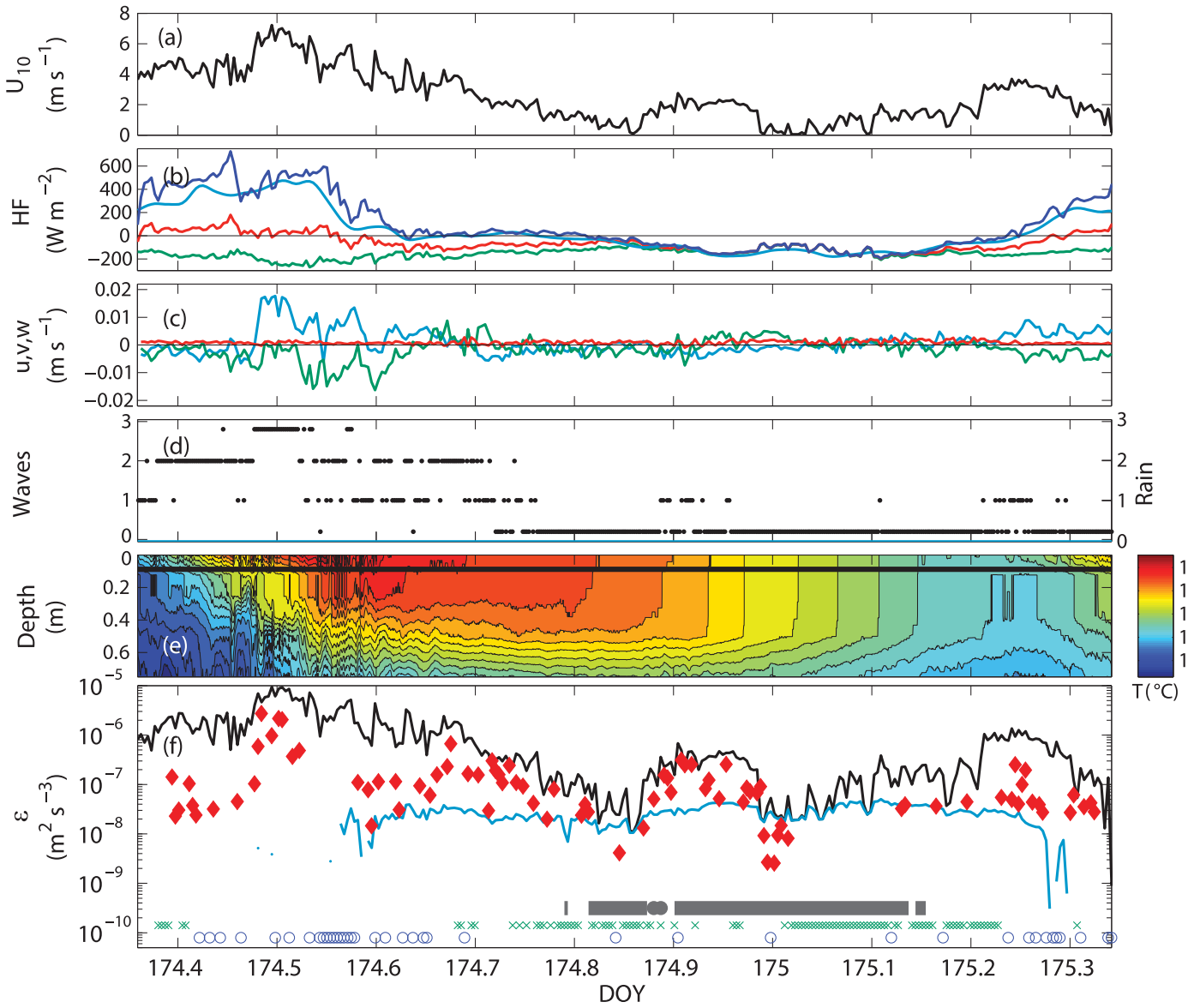

Fig. 6. As for Fig. 5 but days 174.35–175.35.

(e.g., IOC, SCOR and IAPSO, 2010). Lake number, L_N, was computed following Imberger and Patterson (1989). This dimensionless index indicates the extent of tilting of the thermocline, with values greater than 10 indicating minimal tilting, values between 1 and 10 partial tilting, and 1 or less upwelling to the surface. The buoyancy frequency was calculated as $N = (g/\rho_w \, d\rho_w/dz)^{1/2}$.

We computed the depth dependent dissipation rates, ε_z within the surface mixing layer from the surface meteorology and within lake thermistors following Tedford et al. (2014). During cooling, $\varepsilon_z = 0.56 \, u_{*w}^3/(0.4z) + 0.77 \, \beta$ and during heating $\varepsilon_z = 0.6 \, u_{*w}^3/(0.4z)$ where 0.4 is von Karman's constant, z is depth, and β is surface buoyancy flux. u_* and u_{*w} are the friction velocities derived from the relation for shear stress $\tau = \rho_a u_*^2 = \rho_w u_{*w}^2 = \rho_a C_d U^2$ where ρ_a and ρ_w are density of the air and water respectively, U is wind speed, and C_d is the drag coefficient computed at anemometer height and varies with atmospheric stability. For comparisons with the ADV, we let z be the depth of the measurement volume. $\beta = g \, \alpha \, H_*/c_p\rho_w$ where H_* is the effective heat flux in the actively mixing layer, that is, the sum of incoming short wave radiation retained in the actively mixing layer, sensible and latent heat fluxes, and net long wave radiation, g is gravity, α is the thermal expansion coefficient, and c_p is the specific heat of water (Imberger 1985). Besides indicating whether the actively mixing layer is heating or cooling, this approach allows accurate assessment of the sign change in β near the surface. The confidence intervals for

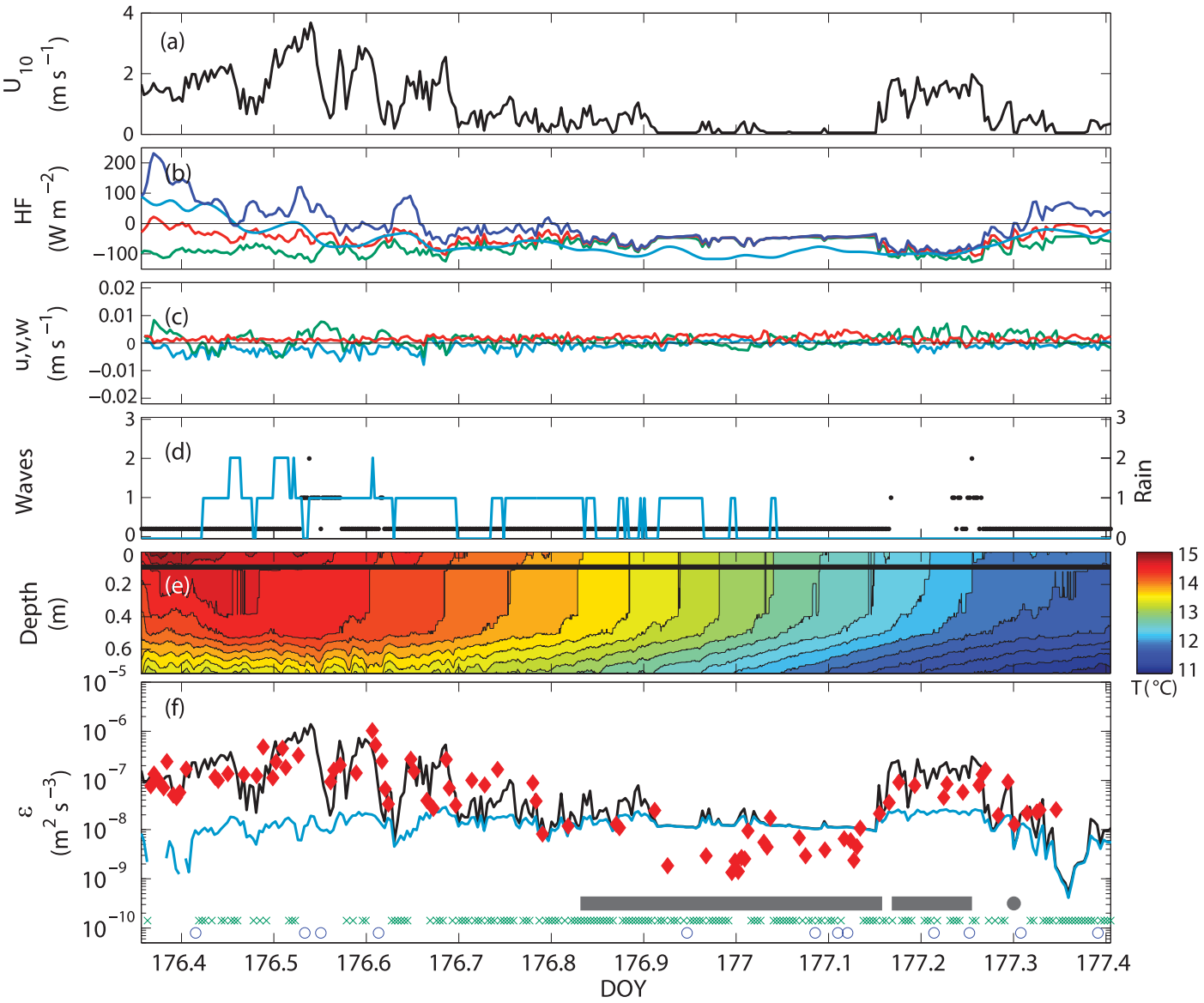

Fig. 7. As for Fig. 4 but for days 176.35–177.4.

the equations in Tedford et al. (2014) are such that ε is computed within a factor of 2.

The Monin–Obukhov length scale for the atmosphere was computed as in MacIntyre et al. (2002) and on the water side of the air–water interface as $L_{MO} = u_{*w}^3/k\beta$ where k is the von Karmon constant. Dissipation is assumed to balance turbulence production. The Monin–Obukhov length scale is the ratio of the production of turbulence by shear to that produced by buoyancy. When negative, heat loss contributes to turbulence. When L_{MO} is negative and shallower than z_{AML}, shear dominates turbulence production at depths above L_{MO} and convection below. If $|L_{MO}|$ is greater than or equal to z_{AML}, the turbulence in the actively mixing is fully energized by wind.

K_z was computed using two approaches. The first was used under cooling and is an extension of Jassby and Powell (1975), and the second was used under heating and follows Osborn (1980). Following Jassby and Powell (1975), we generated an hourly time series of integrated heat flux in layers in the water column and divided by the temperature gradient to obtain K_z. To obtain near surface values, which would otherwise be lost in the integration, we assumed the temperatures at 0.03 m were the same as those at our uppermost measurement depth, 0.01 m. When surface water temperatures were the same as those at the next depth, we let dT/dz be −0.01°C based on examination of data collected using higher resolution temperature sensors (0.002°C accuracy) obtained under cooling (Tedford et al. 2014, S. MacIntyre,

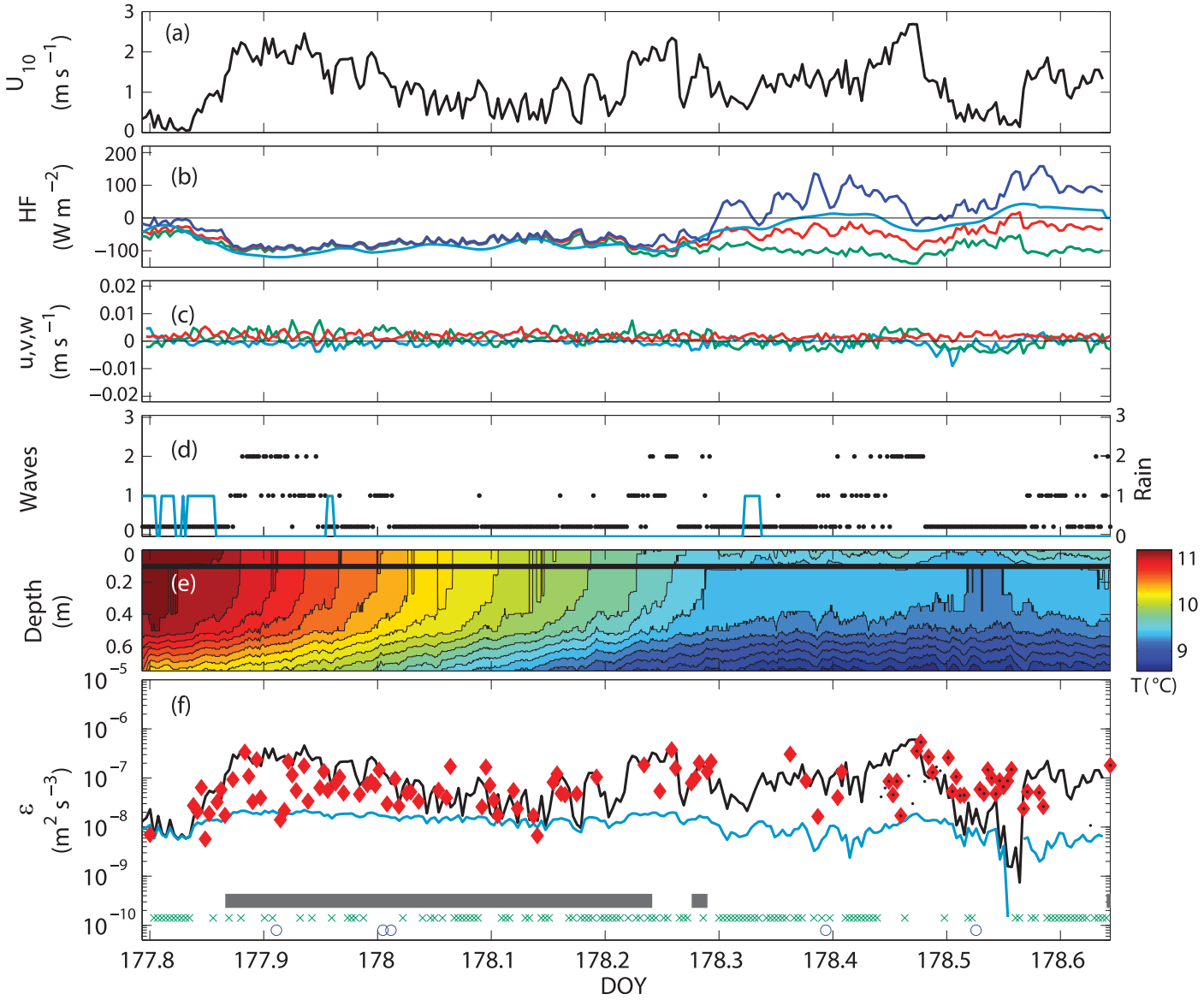

Fig. 8. As for Figs. 4 and 5 but for days 177.8–178.65.

unpublished data) and from microstructure profiling (Jonas et al. 2003). In fact, the gradient at these other locations typically varied between −0.005°C and −0.05°C. Variability results because convection is an unsteady process. The uncertainty in the near-surface temperature gradient implies that K_z can only be discriminated by changes of an order of magnitude. The Jassby and Powell (1975) approach could not be used under heating as the solar radiation term dominated the heat fluxes.

Under heating, we computed K_z following Osborn (1980) as $K_z = R_f/(1-R_f)\ \varepsilon\ N^{-2}$ where $R_f/(1-R_f)$ is computed following Shih et al. (2005) and Bouffard and Boegman (2013). We used this approach within the actively mixing layer and for N up to 25 cycles per hour (cph) for which we found the algorithms for dissipation rate in Tedford et al. (2014) to be applicable (see results). Use of the Osborn (1980) approach assumes that turbulence is being produced locally, be it by shear or buoyancy flux, or turbulence produced elsewhere has been transported to the local site (Ivey and Imberger 1991; Dunckley et al. 2012). For high stratification, $N > 25$ cph, we let K_z be equal to the molecular diffusivity of heat.

In summary, K_z is based on the heat budget method approach under cooling and the Osborn (1980) approach under heating using the equations in Tedford et al. (2014) to obtain dissipation rates as a function of depth. Calculating vertical fluxes using K_z implicitly assumes mixing is occurring in one dimension. As will be seen in the following, horizontal movements occur which moderate the temperature

distribution. Thus, the computed K_z provide an order of magnitude assessment of the magnitude and timing of vertical mixing at the measurement site.

Results

Meteorology

Cloudy conditions prevailed during the study such that maxima in incoming shortwave were low, 200–400 W m^{-2}, on all but 4 d (Fig. 3). Air temperatures had low day to night variation on cloudy days but warmed to $\sim$ 15°C on sunny days with night time lows of 5–10°C. Surface water temperatures were warmer than air temperatures except on three sunny afternoons when they were equal or slightly cooler. Relative humidity was near 100% on cloudy days, and a fine drizzle occurred. On the sunnier days, relative humidity was 40% during the day and 75–80% at night. Winds were northerly on cloudy days with speeds less than 1 m s^{-1}. On the sunnier days, winds tended to be easterly or southerly with maximum wind speeds of 3–6 m s^{-1}. Computed values of the Monin–Obukhov length scale in the atmosphere indicated the atmosphere was unstable except for much of day 172 and for a few hours on day 174 when air temperatures exceeded water temperatures. Air temperatures, relative humidity, and wind direction at the pond site were similar to those measured at the exposed meteorological stations, with air temperatures at the pond occasionally a degree warmer. In contrast, wind speeds, corrected to 10 m, were up to 400% higher at the more exposed site when winds were 1 m s^{-1} at the pond and about 50% higher when winds at the pond were 4 m s^{-1}. Lake numbers frequently dropped to values less than 1 and rose to 10, indicating that the thermocline would up and downwell in response to wind and its relaxation.

Thermal structure and within pond mixing

Temperatures in the pond varied considerably day to day depending on cloud cover and persistence of wind at night (Fig. 3). With the considerable cloud cover at the start of the study, temperatures decreased from 14°C on day 169 to 9°C on day 171. Slight diurnal heating occurred even with reduced solar radiation, as on day 170. Considerable warming occurred in the upper 50 cm on the sunnier days. For example, surface temperatures reached 18°C on day 175. Despite its shallow depth, the water column in the pond was always thermally stratified with temperatures at 0.75 m approximately a degree cooler than at 0.5 m (Fig. 3g). Temperatures increased throughout the water column with increased solar radiation with heating most rapid in the upper water column. This increased heating led to the formation of diurnal thermoclines which downwelled when winds increased followed by upwelling at night when they decreased. In fact, downwelling occurred in response to wind events that caused L_N to drop to values below 1 (days 171, 172, 174, and 175). The depth of the actively mixing layer at night was greater when winds persisted as on days 172, 174, and 175. The coolest near bottom temperatures were found after several cloudy days and the warmest after sunny days. Temperatures began to increase in the upper water column once solar radiation increased near 0400 h. The maxima in near surface water temperatures occurred mid-afternoon after solar radiation had begun to decrease.

The heating and cooling which, along with wind, moderate the near surface changes in temperature, buoyancy frequency, the sign and magnitude of L_{MO}, and mixing within the water column, are presented in Figs. 4–8, times when we had ADV measurements. On calm nights, net surface heat fluxes were ~ -50 W m^{-2} whereas they reached or exceeded values of ~ -150W m^{-2} on nights when winds exceeded 2 m s^{-1} (Fig. 4a,b). Net long wave radiation, LW_{net}, was the primary driver of cooling on calm nights. Values of buoyancy flux under cooling approached -10^{-9} m^2 s^{-3} during the calmest conditions and reached -6×10^{-8} m^2 s^{-3} when winds were highest (Fig. 5a,b). This upper value approaches values of order -10^{-7} m^2 s^{-3} observed on adjacent Toolik Lake when winds and resultant evaporative cooling were higher (MacIntyre et al. 2009*a*). The maximum of total heat input into the pond was $\sim$ 600 W m^{-2} on the sunniest days (Figs. 3, 5b, 6b) and $\sim$ 200 W m^{-2} on the cloudy days (Figs. 4b, 7b, 8b). While solar heating occurred, the much lower positive and sometimes negative values of effective heat flux result because some of the incoming solar passed through to warm the underlying waters and because of near surface losses due to latent and sensible heat fluxes and net long wave radiation, collectively, the net surface heat fluxes. The low values of the effective heat flux and its frequent changes in sign indicated that the upper layer, the surface layer, would be weakly stratified or mixing (Figs. 4b–8b). The heat which accumulated during the day was often less than that computed from the surface energy budget; upwelling of cool water from below often contributed to the difference (Figs. 4b,e, 5b,e, 7b,e, 8b,e). Maxima in heat content in the pond several hours after maximum incoming heat pointed to horizontal flows modifying the heat budget at the measurement station (Fig. 5b).

The buoyancy frequency N varied in the upper 40 cm in response to diel heating and cooling (Fig. 3h). In response to cooling, N decreased to values less than 10 cph at night and increased to values above 20 cph in the day with maximal values of 60 cph on the sunniest days, some of the highest values on record for freshwater systems. Stratification was more persistent in the lower water column, where N tended to be above 20 cph. It increased throughout the water column with downwelling as on the afternoon and into the night of days 172, 174, and 175. The actively mixing layer shoaled with increased N and deepened as it decreased (Fig. 3h). On calm nights, it deepened to $\sim$ 40 cm due to heat loss. Deepening was greater on nights when winds caused

downwelling in the day followed by a decrease in wind speed or shifts in direction.

Due to the primarily cooling conditions of our study, L_{MO} tended to be negative (Fig. 3h). Positive values occurred on sunny days with warm air temperatures. L_{MO} varied in magnitude over diel cycles as the wind increased and decreased. Regardless of whether L_{MO} was negative or positive, it tended to exceed z_{AML} when there were even light winds indicating wind was energizing water at deeper depths. At night when winds decreased below 1 m s^{-1}, z_{AML} had reached its maximum depth, and N was low, L_{MO} decreased to values less than z_{AML}. Non-zero L_{MO} in this case implies that production of near-surface turbulence was dominated by shear.

The depth and intensity of mixing, quantified as K_z, varied over diel cycles (Fig. 3i). Near surface values at night were of order 10^{-3} m^2 s^{-1} and decreased by three orders of magnitude as stratification increased with depth. The depth of the more energetically mixing region was $\sim$ 0.15 m on the nights when winds were light and buoyancy flux was induced primarily by net long wave radiation (Fig. 3h). It extended to nearly 0.4 m as a result of a suite of factors including increased winds, changes in wind direction, or higher winds in the day with accompanying downwelling. In general, L_{MO} was deeper than z_{AML} in the evening. K_z reached its highest values in the lower water column when L_{MO} reached its deepest values, as on the nights of days 172, 174, and 175. On such nights, the temperature gradient in the lower water column decreased as expected with mixing (data not shown). L_{MO} subsequently shoaled as winds dropped near midnight such that it was less than z_{AML} for much of the night. Thus, initial mixing of the actively mixing layer was wind driven, but later, when the winds ceased, mixing was driven by heat loss. Near-surface mixing induced by buoyancy flux alone occurred 20% of the time. Calculated K_z do not capture the variability in near-surface mixing as we assumed, due to the lack of resolution of our temperature loggers, a constant near surface temperature gradient through the night.

K_z decreased by one to two orders of magnitude as near surface waters stratified (Fig. 3i). Near surface values were O10^{-5} m^2 s^{-1} on days with reduced solar heating and one to two orders of magnitude lower on sunny days. K_z tended to decrease with depth, however, it remained above 10^{-5} m^2 s^{-1} below 0.3 m under heating when winds were at least 2 m s^{-1} and $L_{MO} > z_{AML}$. During higher winds, as on days 174 and 175 when L_N decreased to 1 or below, the downwelling and compression of the thermocline increased N such that K_z decreased by an order of magnitude in the lower water column in the afternoon (Figs. 3i, 5e, 6e).

The dynamic response of the thermal structure, near surface flows, and turbulence within the pond to the meteorological forcing is further illustrated in Figs. 4–8. Winds were unsteady with values typically 2 m s^{-1} or higher in the day and tapered at night. Lake numbers typically dropped to values less than 1 with increased wind speeds indicating wind forcing was sufficient to cause the thermocline to tilt and cause upwelling of cool near bottom water (Figs. 3f,5e). In some cases, the thermocline periodically compressed and expanded indicating 2nd vertical mode internal waves (Fig. 5e). Current speeds measured with the ADV were responsive to the magnitude of wind and its direction such that horizontal advection contributed to changes in thermal stratification. For example, the u and v components of velocity each increased to 0.01 m s^{-1} with the southeasterly winds on the morning of day 170 and transported warmed water away from the measurement site (Fig. 4). Thus, conditions in the pond were affected by one dimensional processes, such as heating and cooling, as well as by two dimensional processes including upwelling and wind driven flow.

Acoustic doppler velocimetry

Near surface turbulence, as measured by the ADV, occurred during heating and cooling (Figs. 4–8). Near-surface dissipation rates ranged from 10^{-6} m^2 s^{-3} during highest winds to 10^{-9} m^2 s^{-3} under cooling and light winds. Currents in the u and v directions were of order 0.005–0.01 m s^{-1} when winds were above 1 m s^{-1} and responded within a half hour to increases and decreases. Velocities were measurable but less for lower winds (Figs. 4c–8c). When z_{ADV} was within the actively mixing layer, the turbulence followed or was slightly less than predictions from similarity scaling (Figs. 4f–8f). When the upper water column was stratified to the surface, and turbulence was measurable, ε tended to follow the similarity scaling for $N < 25$ cph (Figs. 3, 4e,f–8e,f). ε was suppressed by at least an order of magnitude relative to predictions from similarity scaling for larger values of N with the suppression of order two orders of magnitude when $N > 40$ cph (Figs. 3h, 6f). Under cooling with negligible winds, dissipation rates either followed similarity scaling or values were up to an order of magnitude lower (Figs. 6f, 7f). Under those conditions, Taylor's hypothesis was often not met indicating the need for another approach to compute turbulence.

β and ε in the absence of wind

To address whether the water column was turbulent under cooling with light to no winds, we computed additional parameters describing turbulence using the data from the ADV. These include the Reynolds stresses, $<u'w'>$ and $<v'w'>$ where the primes indicate fluctuating velocities and $<>$ indicates averaging; vertical velocities; the root mean square of the vertical velocity fluctuations, $w_{rms} = <w'^2>^{1/2}$ and horizontal velocity fluctuations $u_{rms} = <u'^2 + v'^2>^{1/2}$ where the fluctuating velocities were obtained relative to a mean velocity obtained by averaging over 5 min; turbulent Reynolds numbers, $Re_T = w_{rms}h/\upsilon$, where h is mixing layer depth and υ kinematic viscosity; and buoyancy flux at z_{AML} as $\beta_z = w_{rms}^3/h$, where h, the depth of the actively mixing layer, is assumed to scale with the size of the largest eddies

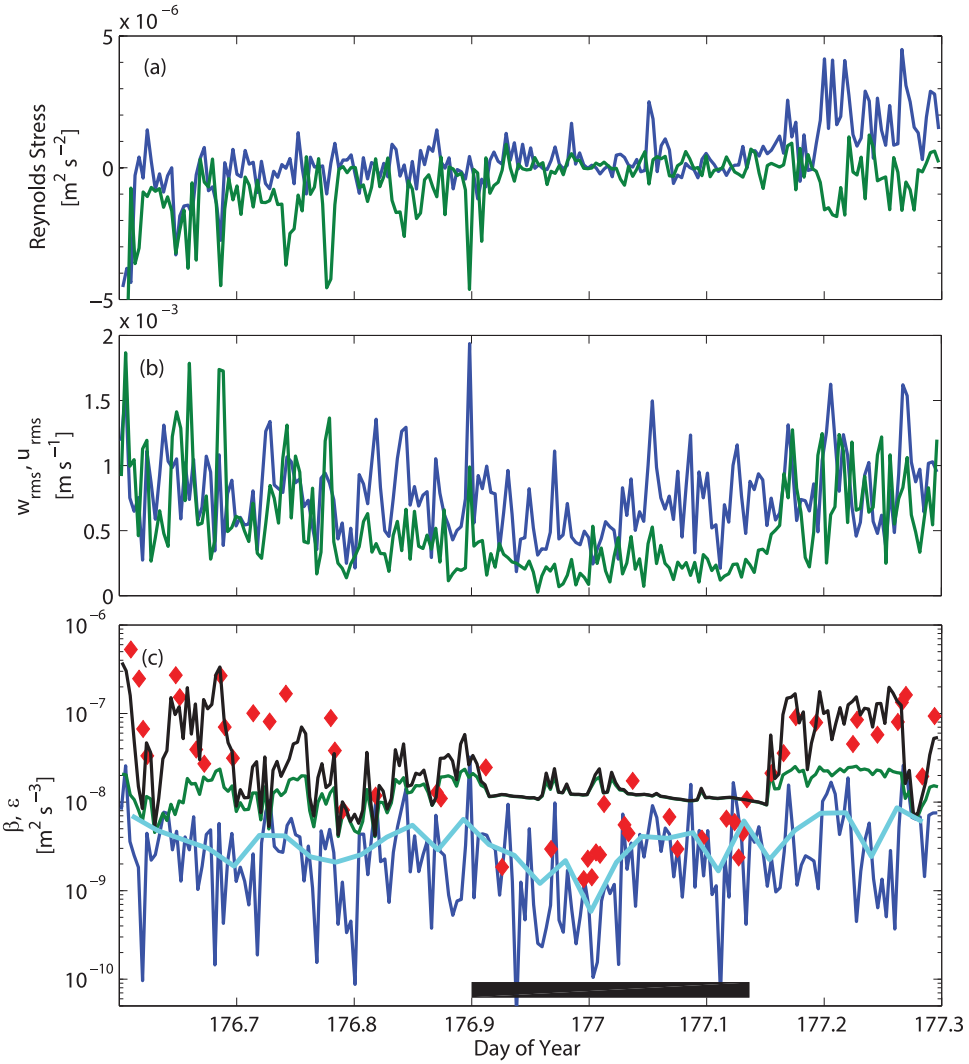

Fig. 9. Time series of (**a**) Reynolds stresses <u′w′> and <v′w′> (blue and green, respectively); (**b**) five-minute averaged w_{rms} (blue) and u_{rms} (green) computed as root mean square velocities from the magnitude of the vertical velocity fluctuations and from the magnitude of the horizontal velocity fluctuations, respectively; (**c**) time series of dissipation rates, ε, from the similarity scaling (black), ε as 0.77β from the surface energy budget (green), β_z as 1-min averages from the vertical velocity fluctuations (blue), 30-min averaged β_z (cyan), and ADV measurements of ε computed as in Figs. 4–8 (red diamonds). Black underbar indicates period with minimal Reynolds stress. During this period with no winds, ε computed from the similarity scaling depends only on buoyancy flux, β.

(Deardorff 1970). For the periods with negligible winds in which we are interested, we let $h = 0.4$ m, the maximum depth at such times. We performed computations for the data in Figs. 4, 6, and 7 but only present results for the latter period (Fig. 9).

The Reynolds stresses indicate the vertical transport of horizontal momentum with negative values for eastward and northward surface stresses, respectively. During afternoon winds, Reynolds stresses were of order 10^{-5} m^2 s^{-2}. When z_{ADV} was within the actively mixing layer or when the upper water column was weakly stratified, the Reynolds stresses were in the direction expected based on wind and, as expected, the square root of the sum of the absolute values of <u′w′> + <v′w′> was equivalent to u_{*w}, the friction velocity on the water side. However, when the upper water column was strongly stratified, as at midday on day 174 (Fig. 6), the direction of the Reynolds stresses was decoupled from that of the wind and the square root of the sum of the absolute values of <u′w′> + <v′w′> was less than u_{*w}. The agreement between the magnitude of u_{*w} measured with the ADV to that computed from wind under weak stratification indicates the magnitude of our measurements of the rms velocities are correct under those conditions.

The magnitude of the Reynolds stresses from late afternoon to early morning were nonzero when there were even light breezes, indicating wind shear produced near surface

turbulence (Fig. 9a). Values decreased to near zero when there was no wind. This decrease indicates that if the near-surface is turbulent, the turbulence would be produced by cooling. Near-surface velocity fluctuations were rapid and nonperiodic and indicated the water surface was turbulent under cooling with and without measurable winds (data not shown). Vertical velocities fluctuated from -3 mm s^{-1} to 6 mm s^{-1}. The root mean square of the vertical velocity fluctuations, $w_{rms} = <w'^2>$ ranged from 0.5 mm s^{-1} to 1.5 mm s^{-1}, and, when winds were negligible, turbulent Reynolds numbers ranged from 250 to just over 1000 and thus were indicative of turbulence. u_{rms} was comparable in magnitude to w_{rms} when the Reynolds stresses exceeded 1×10^{-6} m^2 s^{-2} to 2×10^{-6} m^2 s^{-2}. u_{rms} decreased threefold relative to w_{rms} when Reynolds stresses were near zero and there was no wind (day 176.9 to day 177.15). These differences provide further support for convective cooling driving the turbulence in that interval.

In the following, as a component of validating our measurements of w_{rms}, we compare w_{rms}/w_* with values obtained in modeling and atmospheric studies during convection. w_*, the convective velocity scale, is computed as $w_* = (\beta_0 h)^{1/3}$, where β_0 is surface buoyancy flux. We let h, the depth of the actively mixing layer, have an upper bound of 0.4 m and a lower one of 0.12 m, as mixing was constrained to shallower depths 50% of the time (Fig. 3). For the deeper mixing, w_{rms}/w_* and u_{rms}/w_* equaled 0.3 and 0.1 and for the shallower mixing depth, the ratios were 0.5 and 0.2, respectively. Fredriksson et al. (2016*b*) obtained 0.6 and 0.3, respectively at depths within 20–80% of the surface, depths which encompass our measurements. Following Chou et al. (1986), at our measurement depths and $h = 0.4$ m, $w_{rms}/w_* = 0.7$, similar to Fredriksson et al. (2016*b*). Lenschow et al. (1980), reported in Chou et al. (1986), obtained $w_{rms}/w_* = 0.5$, through much of the actively mixing layer during penetrative convection. Thus, our measurements of w_{rms} with the ADV are reasonable in the context of prior work.

Under cooling, buoyancy flux decays linearly from the surface to the base of the mixing layer (Chou et al. 1986). Our measurement depths were 22–75% of the actively mixing layer depth, β_0 was of order 10^{-8} m^2 s^{-3}, indicating expected values of buoyancy flux at measurement depth, β_z, would be 8×10^{-9} m^2 s^{-3} to 2.5×10^{-9} m^2 s^{-3}. β_z ranged from 10^{-10} m^2 s^{-3} to 5×10^{-8} m^2 s^{-3} during the periods of lightest winds with mean values under cooling of 4.5×10^{-9} m^2 s^{-3} on day 174 to 175 and 3.9×10^{-9} m^2 s^{-3} on day 176–177 (Fig. 9c), within the predicted range. These results indicate that our computed root mean square velocities and β_z are reasonable relative to other studies, the water column was turbulent under pure convection, and dissipation at the air–water interface can be scaled based on buoyancy flux measured from the meteorological data.

In summary, when Reynolds stresses were non-negligible, that is when there were even light winds or currents, predicted values of ε from the similarity scaling and from the ADV measurements were larger than those from surface buoyancy flux under cooling (Figs. 4–9). These results indicate that the turbulence was energized by shear stress under light winds and cooling. When winds had ceased but horizontal currents had not, dissipation rates were elevated above those predicted from surface buoyancy flux. Under cooling with negligible winds, vertical velocity fluctuations were measurable and the magnitude of β_z computed from them was reasonable given the expected linear decay of buoyancy flux with depth. Thus, our calculations indicate continued turbulence under cooling. Shear is the dominant source of near surface turbulence under even the lightest winds, and turbulence is driven purely by convection under cooling conditions when winds and horizontal currents have ceased.

Discussion

The thermal structure, flows, and turbulence within Toolik Small Pond changed dramatically in response to meteorological forcing and were similar to those observed in larger water bodies although on a compressed vertical scale (Brainerd and Gregg 1993; MacIntyre et al. 1999). Maximum heat fluxes were substantial, 600 W m^{-2} on sunny days and 100 W m^{-2} 300 W $^{m-2}$ on cloudy days with nighttime cooling appreciable and ranging from -50 W m^{-2} to -150 W m^{-2}. Also similar to large water bodies, nocturnal mixing at night in the near surface was high, with $K_z \sim= 10^{-3}$ m^2 s^{-1}. However, the depth of near-surface mixing was shallow, and K_z decreased by over two orders of magnitude over distances of a few tens of centimeters. As in larger systems, near-surface mixing was suppressed by the onset of heating. Due to differences in cloud cover, periods with several days of cooling alternated with a period of heating. Lake numbers dropping below 1 with increased wind during the heating period indicate considerable upwelling. For the cooling periods, we will assess whether the upwelling of cool water at night resulted from cooling-induced flows from inshore to offshore as in Bednarz et al. (2009*a*,*b*) or whether up and downwelling of the thermocline occurred and facilitated vertical exchange.

The vertically deployed acoustic Dopper velocimeter successfully quantified near surface velocities and turbulence. Velocities were responsive to changes in wind speed and direction with horizontal velocities often up to 1 cm s^{-1}. When wind energized surface waters, dissipation rates were elevated to values as high as 10^{-6} m^2 s^{-3}, similar to values measured in larger water bodies using microstructure profiling (Brainerd and Gregg 1993; MacIntyre et al. 1999, 2006, 2009*b*). When wind and horizontal currents were negligible, turbulence was caused by cooling and ε of order 10^{-8} m^2 s^{-3}. When horizontal flows persisted during negligible winds, ε was higher than expected from cooling alone indicating shear was the driver of turbulence. In the following,

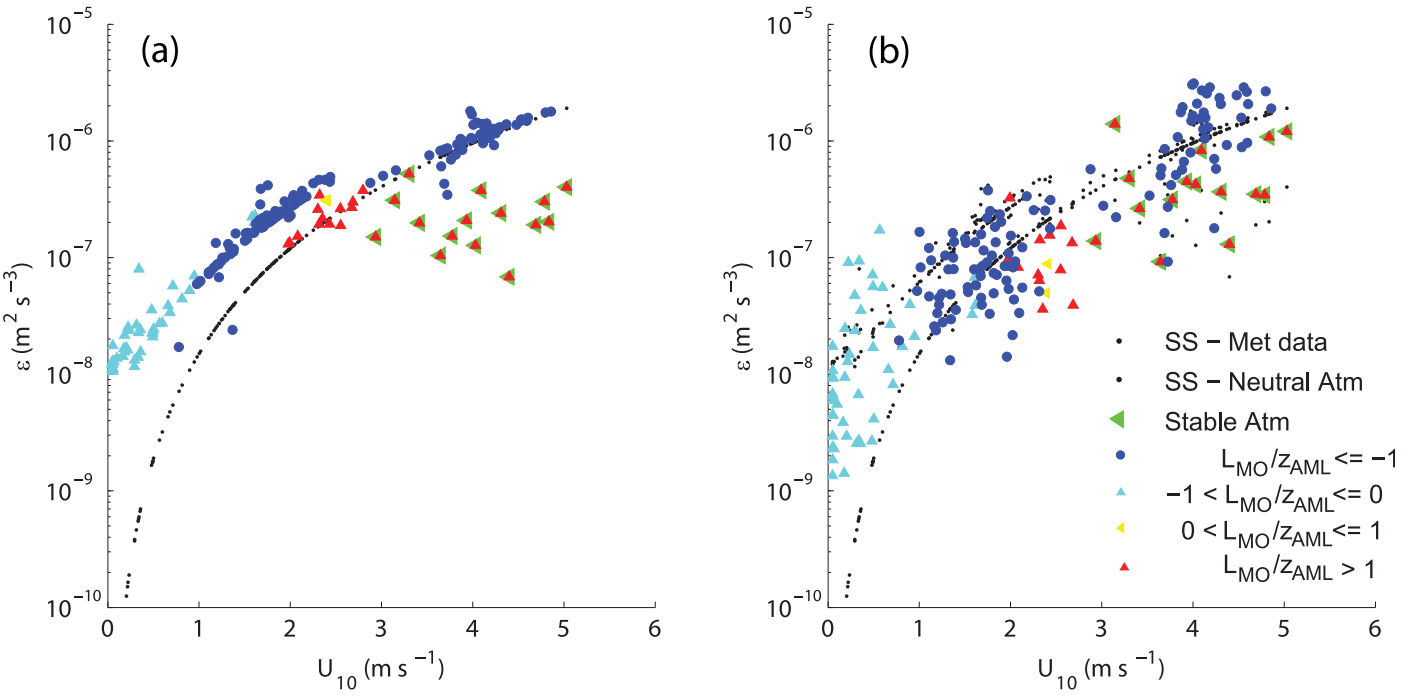

Fig. 10. (**a**) Predicted dissipation rates, ε, calculated from the meteorological and surface water temperature data following Tedford et al. (2014) vs. wind speed at 10 m, U_{10}. Values were computed for times with valid estimates of ε using the ADV data when the measurement volume of the instrument was within the actively mixing layer, z_{AML}. ε was calculated at the depth of the measurement volume: 15 cm for days 171–172 when winds were primarily 2 m s^{-1} or higher and 0.09 m, 0.09 m, and 0.1 m for the following three runs with winds up to 2.5 m s^{-1}. Points underlain by a green arrow represent times with a stable atmosphere. Lower black dotted curve indicates ε for neutral stability computed at 10 cm depth. Calculations are differentiated by the ratio L_{MO}/z_{AML} as described in the legend. (**b**) ε measured with the ADV vs. wind speed at 10 m with values color coded as in *a*. Data are from Figs. 5–8. Upper and lower curves with black dots are expected values from Fig. 10a under the conditions of the experiment and neutral stability, respectively.

we address how well the measured dissipation rates follow the similarity scaling proposed by Tedford et al. (2014). We also compute expected values of the gas transfer coefficient as a function of wind speed and contrast values with other models.

Comparison of measured and predicted dissipation rates

In the following, we contrast values of ε predicted from Tedford et al. (2014) with measured values of ε as a function of wind speed and the stability of the atmosphere and water column (Fig. 10a,b). For the latter, we subdivide the data into four regimes based the on the ratio L_{MO}/z_{AML} with negative values indicating cooling and positive ones heating. For $L_{MO}/z_{AML} < -1$ wind dominates turbulence production in the actively mixing layer, for $-1 < L_{MO}/z_{AML} < 0$, wind only dominates in a shallow near surface layer, for $0 < L_{MO}/z_{AML} < +1$, heating is expected to damp the turbulence but the extent to which it would do so is unknown, and for $L_{MO}/z_{AML} > 1$, wind dominates turbulence production in the actively mixing layer.

The atmosphere was typically unstable except during daytime during days 172 and 174 when winds exceeded 2.5 m s^{-1} (Figs. 5, 6). ε predicted from the surface meteorology under an unstable atmosphere increased with wind speed from 10^{-8} m^2 s^{-3} to 10^{-6} m^2 s^{-3} (Fig. 10a). Calculations are based on the depth of the measurement volume of the ADV, thus the slight depression in predictions for winds above 2.5 m s^{-1} results from the deeper deployment on days 171–172. The enhancement of turbulence under an unstable atmosphere relative to a neutral one is most pronounced for winds less than 2 m s^{-1}. Predicted dissipation rates are up to an order of magnitude lower when the atmosphere was stable as opposed to neutral or unstable. Predicted ε when $L_{MO} > 0$ are independent of the stratification within the pond.

Measured values of dissipation rate followed the same trends as predicted but were variable (Figs. 10b, 11a). When the atmosphere was unstable, values were between those predicted for an unstable and a neutral atmosphere. At the lowest wind speeds, ε was 1 to 3 orders of magnitude above values expected for neutral stability. Measured dissipation rates had a tendency to be less than predicted when winds were 1.5–3 m s^{-1}. This tendency applied to both the regime of $L_{MO}/z_{AML} > 0$ and $L_{MO}/z_{AML} < -1$. The depression may have been a result of upwelling and unsteady winds and currents (Figs. 7, 8). When the atmosphere was stably stratified

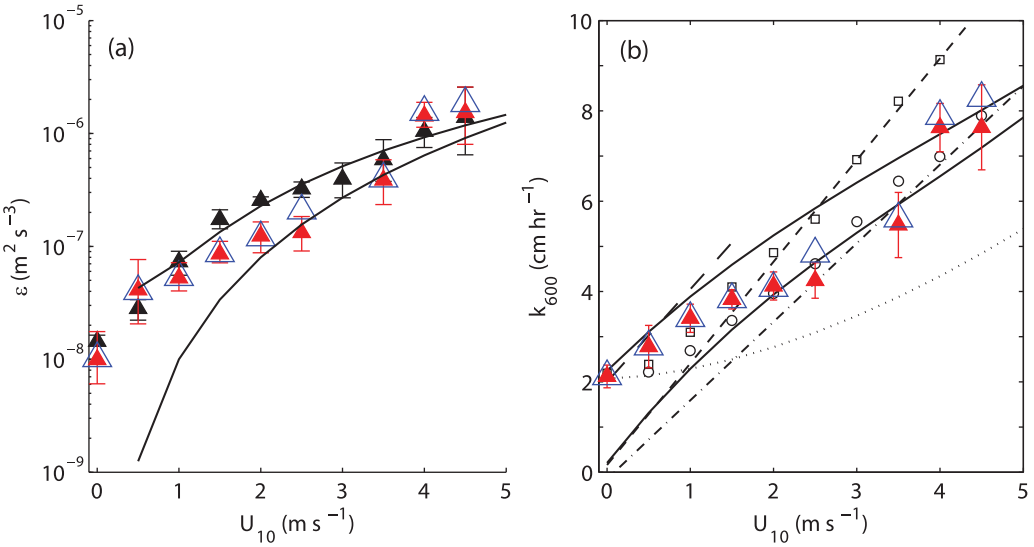

Fig. 11. (**a**) Maximum likelihood estimates (mle) of dissipation rates, ε, against wind speed at 10 m (U_{10}) with data binned at 0.5 m s^{-1} intervals. ε calculated following Tedford et al. (2014) (black triangles, calculations using results and at depths as in Fig. 10a), measured for all conditions (red triangles), and measured during unstable conditions (blue open triangles) using results in Fig. 10b. Upper curve is quadratic fit to the binned ε (black triangles) and lower curve is ε computed for neutral stability. One hundred bootstrapped samples were used in the maximum likelihood estimates with vertical error bars the 95% confidence intervals (Baker and Gibson 1987; MacIntyre et al. 1999) (error bars for unstable conditions are not shown but similar in magnitude). (**b**) Averaged gas transfer coefficient, k_{600}, vs. U_{10} binned as in Fig. 11a. k_{600} was computed using the surface renewal model for all measured ε in Fig. 10b (red triangles) and for unstable or neutral atmosphere (blue open triangles), calculated following Heiskanen et al. (2014) (squares) and Fredriksson et al. (2016*a*) (circles) for the same meteorological conditions as measured ε. Red vertical error bars represent the 95% confidence intervals of the binned averages, computed following Student's *t*-distribution. Upper curve is cubic fit to calculated k_{600} from ε in Fig. 11a under an unstable atmosphere; second curve is cubic fit to k_{600} from ε in Fig. 11a under neutral conditions. Predicted k_{600} from regression equations under cooling (coarse dashed line), for heating and cooling (fine dashed line), and for heating (dash dot line) in MacIntyre et al. (2010); dotted line is k_{600} following Cole and Caraco (1998).

and $L_{MO}/z_{AML} > 1$, measured dissipation rates were similar to or up to an order of magnitude higher than predictions. Dissipation rates tended to be slightly above predictions for unstable atmospheres for wind speeds above 4 m s^{-1} (Figs. 10b, 11a).

The overall good congruence between measured and predicted dissipation rates validates the similarity scaling in Tedford et al. (2014) although the somewhat lower measured ε for winds between 1.5 m s^{-1} and 3 m s^{-1} implies some moderation either related to unsteady winds or by processes occurring within the water column not included in the meteorologically based equations. The results indicate that the use of drag coefficients from local, as opposed to upwind, conditions was appropriate. They also imply that the possible increase in drag coefficients at low winds, as reviewed in Csanady (2001) and Wüest and Lorke (2003), is incorporated adequately by the increased drag coefficients due to an unstable atmosphere.

Cooling and near-surface turbulence

The contribution of cooling to near surface turbulence has been the subject of numerous papers, with its contribution quantified by the turbulent velocity scale from cooling, w_*, obtained from the buoyancy flux (Imberger 1985; MacIntyre et al. 2002, 2010; Read et al. 2012) or from buoyancy flux directly (Tedford et al. 2014; Fredriksson et al. 2016*a*,*b*). Values of u_{*w}, the water friction velocity, and w_* both tended to be low and comparable in magnitude, $\sim$ 0.002 m s^{-1}, for much of the study (data not shown). With persistent cloud cover, w_* was often non-zero during the day. Maximal values of w_*, 0.003 m s^{-1}, occurred either on clear nights when winds were light or during higher winds. In the first case, turbulence was driven by net long wave radiation. For the second, u_{*w} was twice as high. During periods of heating when w_* was zero and winds were elevated, u_{*w} ranged from 0.003 m s^{-1} to 0.008 m s^{-1}. Periods of calm under cooling, identified as wind speeds less than or equal to 0.15 m s^{-1}, occurred 20% of the time. The ratio of u_{*w}/w_* during periods when w_* was positive equaled 1.3, similar to values for much larger lakes in Read et al. (2012), and had maxima during windy periods of 10. Horizontal momentum fluxes persisted for short periods after winds ceased such that shear persisted and dissipation continued to follow law of the wall scaling. Only when winds had died down for periods of a half hour or longer did pure convection occur in which buoyancy flux dominated turbulence production. Thus, in contrast to predictions in Read et al. (2012), we show here that shear dominates near-surface turbulence

production under cooling most of the time even for a small pond. However, once wind and horizontal currents have ceased, convection can drive the turbulence.

The surface renewal model

Gas transfer coefficients can be computed from dissipation rates using the surface renewal model: $k_{600} = c_1(\varepsilon\upsilon)^{1/4} S_c^{-1/2}$ where S_c, the Schmidt number, equal to 600 normalizes values to those for CO_2 at 20°C, υ is kinematic viscosity, and c_1 is a coefficient. The small eddy model version of the surface renewal model, as shown here, applies to flows where the turbulent Reynolds number is greater than 500 and assumes that c_1 has a fixed value (see review in MacIntyre et al. 1995). Based on theoretical grounds, its value is 0.4 (Lamont and Scott 1970). Empirical and modeling efforts indicate c_1 ranges from 0.2 to 1, and despite the earlier formalism, that its magnitude may depend on turbulence for $\varepsilon > \sim 5 \times 10^{-6}$ m^2 s^{-3} as well as depth and the cleanliness of the water surface (Zappa et al. 2007; Wang et al. 2015; Fredriksson et al. 2016*b*). In the following, as our dissipation rates are lower than the threshold in Wang et al. (2015), we chose a value near the mean in field studies and let $c_1 = 0.5$.

Gas transfer coefficients computed from our measured dissipation rates tended to have values similar to predictions for an unstable atmosphere for winds less than 2 m s^{-1} and values intermediate to those for an unstable and a neutral atmosphere at higher winds (Fig. 11b). Our averaged k_{600} were similar to predictions in the modeling by Fredriksson et al. (2016*a*) who included shear and convection in their direct numerical simulations. These processes dominate turbulence production in small ponds with reduced influence of surface waves. At winds above 2.5 m s^{-1}, both followed the regression equation under heating in MacIntyre et al. (2010). At low winds, our predictions are similar to those of Fredriksson et al. (2016*a*) and Heiskanen et al. (2014). Fredriksson et al. (2016*a*) predict that convection will combine with shear leading to higher values of k_{600} than from shear alone when a Richardson number, defined as $\mathrm{Ri} = \beta v/u_{*w}^4$, exceeds 0.004. Using $u_{\star w}$ and β from our data set under cooling conditions, enhancement relative to neutral stability is seen for winds below the computed threshold of 1.1 m s^{-1} (Fig. 11b). Heiskanen et al. (2014) also included shear and buoyancy flux in their algorithm for k_{600} with coefficients obtained by inverse procedures from eddy covariance (EC) data. The similarity of results at light winds supports our use of $c_1 \sim = 0.5$. At higher winds, predictions from Heiskanen et al (2014) exceed those for an unstable atmosphere and are similar to the predictions in MacIntyre et al. (2010) for combined heating and cooling. This correspondence at higher wind speeds may be due to a greater influence of surface waves or currents in the larger lakes for which the equations were derived.

Values of k_{600} higher than predicted for a neutral atmosphere result from the greater momentum transfer from wind to water when the atmosphere is unstable, shear from residual currents as winds ceased, and turbulence from convection alone. At the lowest wind speeds, the three studies all predict $k_{600} = 2$ cm h^{-1}. Such would also be obtained under convection for the buoyancy fluxes in this study (Fig. 9). For the range of wind speeds in this study and within the actively mixing layer, k_{600} estimated from the ADV measurements of ε tended to follow the predictions for k_{600} computed with ε from similarity scaling with variability due to changes in the stability of the atmosphere and water column.

Effects of stratification on near-surface turbulence

Our study has focused on comparisons of predicted and measured turbulence when the measurement volume of the ADV was within the actively mixing layer, here typically from late afternoon through early morning. The observations in Figs. 4–8 indicate that the similarity scaling provided accurate predictions up to conditions of moderate stratification, that is, up to $N \sim = 25$ cph, even when the measurement volume was no longer within the actively mixing layer. For greater stratification, dissipation rates were suppressed relative to values expected near the surface. While our predicted ε indicate that atmospheric stability leads to reduced turbulence, measured values were sometimes higher than predictions even when $L_{MO} > 1$ (Fig. 10a,b). Insufficient data have been collected to quantify how near-surface turbulence changes in response to surface stratification. That is, additional effort is required to quantify the regime of heating with light winds when $0 < L_{MO} < 1$ and the regime of heating with stronger winds. Increased near surface shear is expected (McGillis et al. 2004).

Diel variations in the stability of the atmosphere and within ponds and lakes will contribute to between site differences. For example, 12 h k_{600} from ponds in temperate regions tend to be lower than we compute (Holgerson et al. 2017). For winds of $\sim$ 2 m s^{-1}, Clark et al. (1995) obtained average values ranging from 0.5 cm h^{-1} to 3 cm h^{-1} at a larger pond. The atmosphere was unstable for much of our experiment, whereas a stable atmosphere during the day is more likely in summer for the temperate ponds and the upper water column is likely be stratified. Predictions following the wind-based equation of Cole and Caraco (1998), whose algorithm is based on tracer experiments which average periods of heating and cooling, are nearly a factor of two lower at all but the lowest wind speeds (Fig. 11b). This discrepancy may also result from variability in stratification. Thus, as discussed above, between site differences in k_{600} may result from differences in atmospheric and near surface stability in the water column. Pond and lake size dependent variability in these attributes may prove a stronger predictor of k_{600} than the expected lake-size dependence on the magnitude of surface waves and cooling as suggested by Vachon and Prairie (2013) and Read et al. (2012).

Routine meteorological measurements coupled with surface water temperatures and basic equations for the drag and mass transfer coefficients that take into account atmospheric stability enable accurate predictions of dissipation rates and the gas transfer coefficient over lakes and ponds with light winds. Dissipation rates were dependent upon near surface shear except during brief periods when winds ceased. When winds were negligible under cooling, β was O 10^{-8} m^2 s^{-3} and $k_{600} = 2$ cm h^{-1} (Fig. 11). Additional work is required to quantify dissipation rates and k_{600} when $L_{MO} > 0$. When winds were negligible under heating, the upper water column stratified. In such conditions, wind induced shear would cease and appreciable near-surface turbulence and nonzero k_{600} are expected only if there are residual currents (Fig. 5, day 171.64 and 172.3). At higher winds speeds, white capping and breaking of surface waves increase ε above predictions from law of the wall scaling in larger water bodies (Terray et al. 1996; Turney 2016; Moghimi et al. 2016). It is not known whether the fetch is sufficient in small ponds for sufficient wave development for a similar intensification of turbulence.

Conditions enabling vertical and horizontal exchanges

Exchanges between the lower and upper water column induced by processes occurring in two dimensions will occur if horizontal convective circulations develop (Lei and Patterson 2005; Bednarz et al. 2009*a*) or with appreciable tilting of the thermocline as expected with low Lake numbers. Inshore water can also flow downslope from a process known as differential cooling also initiated when shallow regions cool more rapidly than offshore waters (Monismith et al. 1990). Over several days with cloudy conditions, the pond slightly warmed in the day but the overall trend was one in which temperatures decreased (Fig. 3). Shortly after the cessation of heating, temperatures below the actively mixing layer sometimes decreased and sometimes increased more rapidly than in the overlying water. To test whether the more rapid rate of cooling resulted from gravity currents from inshore, we calculated flow speeds resulting from cooling at shallower inshore sites following Fischer et al. (1979) and using a typical heat flux for such periods, -50 W m^{-2}, and light winds, 1 m s^{-1}. Computed flow speeds were 0.002 m s^{-1} using a bottom drag coefficient of 0.5 as appropriate for flat plates and Reynolds number, Re, of O(1000). $\mathrm{Re} = ul/\upsilon$ with l the depth of the actively mixing layer. It would take over an hour to flow 10 m. The decreases in temperature below the actively mixing layer occurred quickly and typically during periods of calm following events when either L_N had dropped to values near 1 or winds had shifted direction. Consequently, it is more likely that decreasing water temperatures at the measurement site resulted from upwelling of cooler water from deeper depths. The mixing induced by cooling of the upper water column would enable exchange between the upper and lower column (Fig. 3).

During sunny conditions, internal wave motions were also prevalent and enabled vertical and horizontal exchanges. Diurnal thermoclines formed and downwelled when winds increased and values of L_N dropped below 1 (Figs. 3, 5, and 6). Upwelling of deeper water would have occurred away from our measurement site. Horizontal flows increased in response to the wind-forced second vertical mode wave mid-day day 171 (Fig. 5c,e). The mid-water column separation of isotherms on the afternoon of day 174 as winds dropped and changed direction also indicates advective flow (Fig. 3, 6). $L_N \leq 1$ is associated with increased dissipation rates from internal wave induced mixing (Horn et al. 2001; Boegman et al. 2005; MacIntyre et al. 2009*b*). However, we obtain K_z of molecular rates using the measured dissipation rates, N equal to 50 cph, and the algorithms in Shih et al. (2005) and Bouffard and Boegman (2013) despite nonlinear internal wave activity (Figs. 3, 5). Thus, enhanced fluxes to the surface can occur via upwelling but are not expected within strongly stratified, downwelled diurnal thermoclines. Accurately quantifying emissions of greenhouse gases from small ponds requires chamber measurements over diel cycles at multiple locations in order to take into account the spatial and temporal variability of processes which would bring dissolved gases to the air–water interface.

Sheltering from wind

The reduced wind speeds over the pond relative to the exposed site 250 m away indicate it was sheltered. Under heating during the sunny period, morning winds over the pond were generally 1 m s^{-1} vs. 2 to 4 m s^{-1} at the exposed site. The low winds coupled with a relatively high diffuse attenuation coefficient, $k_d \sim= 1$ m^{-1}, enabled shallow, strongly stratified diurnal thermoclines. For two of the three windy afternoons, Lake numbers were similar when computed using wind speeds from the pond and lake meteorological stations whereas, on day 176, the values of L_N differed being 1 and 0.1, respectively. Thus, the sheltering can reduce wind speeds over ponds and the potential for upwelling and mixing as expected with low L_N (MacIntyre et al. 2009*a*,*b*). Under cooling, buoyancy fluxes computed using data from the exposed meteorological station were up to five times higher than those computed using the data from the pond site, and the periods with negligible winds were longer at the pond. Thus, the decreased winds in sheltered locations enable strong near surface stratification, reduce the extent of upwelling and likelihood of downslope gravity currents, and limit the depth of mixing under cooling conditions such that persistent stratification occurs at shallow depths.

Hydrodynamic modeling of ponds which takes into consideration the diminution of wind due to sheltering, bottom slope as it moderates any downslope flows, and pond size as it influences Lake numbers would enable prediction of the frequency of events which bring oxygenated waters from

shallow areas to deeper sites and ventilation of the lower water column. This information is needed to quantify conditions favoring methane oxidation and the frequency of events supplying climate-forcing trace gases to the air–water interface for these numerically important water bodies.

In summary, the mixing dynamics in small ponds are similar to those in larger water bodies but on a compressed vertical scale. Near surface waters are turbulent, and ε can be quantified using acoustic Doppler velocimetry even during stratified conditions and with light winds. Dissipation rates are well predicted from the similarity scaling in Tedford et al. (2014) developed for a 4 km^2 lake. The unstable atmosphere found under cooling conditions augments turbulence under light winds as does convection when winds cease. Unsteady winds contribute to variability in dissipation rates. Turbulence can be computed based on wind shear except when winds have ceased for a half hour or more and horizontal flows decay in which case convection alone induces turbulence. Latent and sensible heat fluxes are negligible as winds approach zero, and the net heat losses associated with long wave radiation provide the energy for mixing at such times. Thus, mixing by convection alone is more likely under calm, clear sky conditions. Wind speeds and thermal stratification in this study were similar to those measured in the vicinity of subarctic and arctic ponds during summer (Laurion et al. 2010; Deshpande et al. 2015). Measurements similar to these and combined with chamber studies in other thaw ponds, some of which are sheltered from wind and some which have a long fetch, will lead to accurate predictions of mixing events which bring dissolved gases to the air–water interface and gas transfer coefficients for these abundant water bodies with high concentrations of CO_2 and CH_4. Besides applying to larger lakes on which the equations for dissipation rates were developed (Tedford et al. 2014), the similarity scaling is applicable to other small water bodies and wetlands with low wind speeds (Walter Anthony and MacIntyre 2016). Thus, these analyses of the extent of turbulence during heating and cooling provide a basis for improved computation of gas fluxes from pond and lake sites.

References

Adams, E. E., D. J. Cosler, and R. Helfrich. 1990. Evaporation from heated water bodies: Predicting combined forced plus free convection. Water Resour. Res. **26**: 425–435. doi:10.1029/WR026i003p00425

Baker, M. A., and C. H. Gibson. 1987. Sampling of turbulence in the stratified ocean: Statistical consequences of strong intermittency. J. Phys. Oceanogr. **17**: 1817–1836. doi:10.1175/1520-0485(1987)017<1817:STITSO>2.0.CO;2

Bednarz, T. P., C. Lei, and J. C. Patterson. 2009*a*. Unsteady natural convection induced by diurnal temperature changes in a reservoir with slowly varying bottom topography. Int. J. Therm. Sci. **48**: 1932–1942. doi:10.1016/j.ijthermalsci.2009.02.011

Bednarz, T. P., C. Lei, and J. C. Patterson. 2009*b*. A numerical study of unsteady natural convection induced by isoflux surface cooling in a reservoir model. Int. J. Heat Mass Tran. **52**: 56–66. doi:10.1016/j.ijheatmasstransfer.2008.06.029

Bouffard, D., and L. Boegman. 2013. A diapycnal diffusivity model for stratified environmental flows. Dyn. Atmos. Oceans **61–62**: 14–34. doi:10.1016/j.dynatmoce.2013.02.002

Boegman, L., G. N. Ivey, and J. Imberger. 2005. The degeneration of internal waves in lakes with sloping topography. Limnol. Oceanogr. **50**: 1620–1637. doi:10.4319/lo.2005.50.5.1620

Brainerd, K., and M. C. Gregg. 1993. Diurnal restratification and turbulence in the oceanic surface mixed layer. J. Geophys. Res. **98**: 22645–22656. doi:10.1029/93JC02297

Chen, C. T., and J. Millero. 1977. The use and misuse of pure water PVT properties for lake waters. Nature **266**: 707–708. doi:10.1038/266707a0

Chou, S.-H., D. Atlas, and E.-N. Yeh. 1986. Turbulence in a convective marine atmospheric boundary layer. J. Atmos. Sci. **43**: 547–564. doi:10.1175/1520-0469(1986)043<0547:TIACMA>2.0.CO;2

Clark, J. F., P. Schlosser, R. Wanninkhof, H. J. Simpson, W. S. F. Schuster, and D. T. Ho. 1995. Gas transfer velocities for SF_6 and ^3He in a small pond a low wind speeds. Geophys. Res. Lett. **22**: 93–96. doi:10.1029/94GL02410

Cole, J. J., and N. F. Caraco. 1998. Atmospheric exchange of carbon dioxide in a low-wind oligotrophic measured by the addition of SF_6. Limnol. Oceanogr. **43**: 647–656. doi:10.4319/lo.1998.43.4.0647

Crevecoeur, S., W. F. Vincent, J. Comte, and C. Lovejoy. 2015. Bacterial community structure across environmental gradients in permafrost thaw ponds: Methanotroph-rich ecosystems. Front. Microbiol. **6**: 1–15. doi:10.3389/fmicb.2015.00192

Crevecoeur, S., W. F. Vincent, and C. Lovejoy. 2016. Environmental selection of planktonic methanogens in permafrost thaw ponds. Sci. Rep. **6**: 1–10. doi:10.1038/srep31312

Csanady, G. T. 2001. Air-sea interaction: Laws and mechanisms. Cambridge Univ. Press.

Davis, K. A., and S. G. Monismith. 2011. The modification of bottom boundary layer turbulence and mixing by internal waves shoaling on a barrier reef. J. Phys. Oceanogr. **41**: 2223–2241. doi:10.1175/2011JPO4344.1

Deardorff, J. W. 1970. Convective velocity and temperature scales for unstable planetary boundary layer and for Rayleigh convection. J. Atmos. Sci. **27**: 1211–1213. doi:10.1175/1520-0469(1970)027<1211:CVATSF>2.0.CO;2

Deshpande, B. N., S. MacIntyre, A. Matveev, and W. F. Vincent. 2015. Oxygen dynamics in permafrost thaw

lakes: Anaerobic bioreactors in the Canadian subarctic. Limnol. Oceanogr. **60**: 1656–1670. doi:10.1002/lno.10126

Downing, J. A. 2009. Global limnology: Up-scaling aquatic services and processes to planet Earth. Verh. Int. Verein. Limnol. **30**: 1149–1166. doi:10.1080/03680770.2009.11923903

Downing, J. A., and others. 2006. The global abundance and size distribution of lakes, ponds, and impoundments. Limnol. Oceanogr. **51**: 2388–2397. doi:10.4319/lo.2006.51.5.2388

Dunckley, J. F., J. R. Koseff, J. V. Steinbuck, S. G. Monismith, and A. Genin. 2012. Comparison of mixing efficiency and vertical diffusivity models from temperature microstructure. J Geophys. Res. **117**. doi:10.1029/2012JC007967

Fairall, C. W., E. F. Bradley, D. P. Rogers, J. B. Edson, and G. S. Young. 1996. Bulk parameterization of air-sea fluxes for tropical ocean-global atmosphere coupled-ocean atmosphere response experiment. J. Geophys. Res. **101**: 3747–3764. doi:10.1029/95JC03205

Fredriksson, S. T., L. Arneborg, H. Nilsson, and R. A. Handler. 2016*a*. Shear stress dependence of gas transfer velocity equations using DNS. J. Geophys. Res. Oceans **121**: 7369. doi:10.1002/2016JC011852

Fredriksson, S. T., L. Arneborg, H. Nilsson, Q. Zhang, and R. A. Handler. 2016*b*. An evaluation of gas transfer velocity parameterizations during natural convection using DNS. J. Geophys. Res. Oceans **121**: 1400. doi:10.1002/2015JC011112

Fischer, H. B., E. J. List, R. C. Y. Koh, J. Imberger, and H. Brooks. 1979. Mixing in inland and coastal waters. 2nd ed.. Academic Press.

Gålfalk, M., D. Bastviken, S. Fredriksson, and L. Arneborg. 2013. Determination of the piston velocity for water-air interfaces using flux chambers, acoustic Doppler velocimetry, and IR imaging of the water surface. J. Geophys. Res. Biogeosci. **118**: 770–782. doi:10.1002/jgrg.20064

Heiskanen, J. J., I. Mammarella, S. Haapanala, J. Pumpanen, T. Vesala, S. MacIntyre, and A. Ojala. 2014. Effects of cooling and internal wave motions on gas transfer coefficients in a boreal lake. Tellus B 2014. **66**: 22827. doi:10.3402/tellusb.v66.22827

Holgerson, M. A., and P. A. Raymond. 2016. Large contribution to inland water CO_2 and CH_4 emissions from very small ponds. Nat. Geosci. **9**: 222. doi:10.1038/NGEO2654

Holgerson, M. A., E. R. Farr, and P. A. Raymond. 2017. Gas transfer velocities in small forested ponds. J. Geophys. Res. Biogeosci. **122**: 1011. doi:10.1002/2016JG003734

Horn, D. A., J. Imberger, and G. N. Ivey. 2001. The degeneration of large-scale interfacial gravity waves in lakes. J. Fluid Mech. **434**: 181–2071. doi:10.1017/S0022112001003536

Imberger, J. 1985. The diurnal mixed layer. Limnol. Oceanogr. **30**: 737–770. doi:10.4319/lo.1985.30.4.0737

Imberger, J., and J. C. Patterson. 1989. Physical limnology. Adv. Appl. Mech. **27**: 303–475. doi.org/10.1016/S0065-2156(08)70199-6

IOC, SCOR and IAPSO. 2010. The international thermodynamic equation of seawater–2010: Calculation and use of thermodynamic properties. Intergovernmental Oceanographic Commission, Manuals and Guides No. 56, UNESCO (English). Available from http://www.TEOS-10.org. See appendix A.20 and appendix K of the TEOS-10 Manual.

Ivey, G. N., and J. Imberger. 1991. On the nature of turbulence in a stratified fluid. Part 1: The efficiency of mixing. J. Phys. Oceanogr. **21**: 659–658. doi:10.1175/1520-0485(1991)021<0659:OTNOTI>2.0.CO;2

Jassby, A., and T. M. Powell. 1975. Vertical patterns of eddy diffusion during stratification in Castle Lake, California. Limnol. Oceanogr. **38**: 1008–1019. doi:10.4319/lo.1975.20.4.0530

Jonas, T., A. Stips, W. Eugster, and A. Wüest. 2003. Observations of a quasi shear-free lacustrine convective boundary layer: Stratification and its implications on turbulence. J. Geophys. Res. **108**. doi:10.1029/2002JC001440

Lamont, J. C., and D. S. Scott. 1970. An eddy cell model of mass transfer into the surface of a turbulent liquid. J. Am. Inst. Chem. Eng. **16**: 513–519. doi:10.1002/aic.690160403

Laurion, I., W. F. Vincent, S. MacIntyre, L. Retamal, C. Dupont, P. Francus, and R. Pienitz. 2010. Variability in greenhouse gas emissions from permafrost thaw ponds. Limnol. Oceanogr. **55**: 115–133. doi:10.4319/lo.2010.55.1.0115

Lei, C., and J. C. Patterson. 2005. Unsteady natural convection in a triangular enclosure induced by surface cooling. Int. J. Heat Fluid Flow **26**: 307–321. doi: doi.org/10.1016/j.ijheatfluidflow.2004.08.010

Lenschow, D. H., J. C. Wyngaard, and W. T. Pennell. 1980. Mean-field and second-moment budgets in a baroclinic, convective boundary layer. J. Atmos. Sci. **37**: 1313–1326. doi:10.1175/1520-0469(1980)037<1313:MFASMB>2.0.CO;2

Liu, H., Q. Zhang, G. G. Katul, J. J. Cole, F. S. Chapin, and S. MacIntyre. 2016. Large CO_2 effluxes at night and during synoptic weather events significantly contribute to CO_2 emissions from a reservoir. Environ. Res. Lett. **11**: 064001. doi:10.1088/1748-9326/11/6/064001

Lombardo, C., and M. Gregg. 1989. Similarity scaling of viscous and thermal dissipation in a convecting surface boundary layer. J. Geophys. Res. **94**: 6273–6284. doi:10.1029/JC094iC05p06273

MacIntyre, S., R. Wanninkhof, and J. P. Chanton. 1995. Trace gas exchange across the air-water interface in freshwater and coastal marine environments, p. 52–97. *In* P. A. Matson and R. C. Harriss [eds.], Methods in ecology, biogenic trace gases: Measuring emissions from soil and water. Blackwell Science.

MacIntyre, S., K. M. Flynn, R. Jellison, and J. R. Romero. 1999. Boundary mixing and nutrient flux in Mono Lake, CA. Limnol. Oceanogr. **44**: 512–529. doi:10.4319/lo.1999.44.3.0512

MacIntyre, S., J. R. Romero, and G. W. Kling. 2002. Spatial-temporal variability in mixed layer deepening and lateral advection in an embayment of Lake Victoria, East Africa. Limnol. Oceanogr. **47**: 656–671. doi:10.4319/lo.2002.47.3.0656

MacIntyre, S., J. O. Sickman, S. A. Goldthwait, and G. W. Kling. 2006. Physical pathways of nutrient supply in a small, ultra-oligotrophic lake during summer stratification. Limnol. Oceanogr. **51**: 1107–1124. doi:10.4319/lo.2006.51.2.1107

MacIntyre, S., J. P. Fram, P. J. Kushner, N. D. Bettex, W. J. O'brien, J. E. Hobbie, and G. W. Kling. 2009*a*. Climate-related variations in mixing dynamics in an Alaskan arctic lake. Limnol. Oceanogr. **54**: 2401–2417. doi:10.4319/lo.2009.54.6_part_2.2401

MacIntyre, S., J. F. Clark, R. J. Jellison, and J. P. Fram. 2009*b*. Turbulent mixing induced by non-linear internal waves in Mono Lake, CA. Limnol. Oceanogr. **54**: 2255–2272. doi:10.4319/lo.2009.54.6.2255

MacIntyre, S., A. J. Jonsson, M. Jansson, J. Aberg, D. Turney, and S. Miller. 2010. Buoyancy flux, turbulence, and the gas transfer coefficient in a stratified lake. Geophys. Res. Lett. **37**. doi:10.1029/2010GL044164

MacIntyre, S., J. R. Romero, G. M. Silsbe, and B. M. Emery. 2014. Stratification and horizontal exchange in Lake Victoria, East Africa. Limnol. Oceanogr. **59**: 1805–1838. doi:10.4319/lo.2014.59.6.1805

Matveev, A., I. Laurion, B. N. Deshpande, N. Bhiry, and W. F. Vincent. 2016. High methane emissions from thermokarst lakes in subarctic peatlands. Limnol. Oceanogr. **61**: S150–S164. doi:10.1002/lno.10311

Mammarella, I., A., and others. 2015. Carbon dioxide and energy fluxes over a small lake in southern Finland. J. Geophys. Res. Biogeosci. **120**: 1296–1314. doi:10.1002/2014JG002873

McGillis, W. R., and others. 2004. Air-sea CO_2 exchange in the equatorial Pacific. J. Geophys. Res. **109**. doi:10.1029/2003JC002256

Moghimi, S., J. Thomson, T. Ozkan-Haller, L. Umlauf, and S. Zippel. 2016. On the modeling of wave-enhanced turbulence nearshore. Ocean Model. **103**: 118–132. doi:10.1016/j.ocemod.2015.11.004

Monismith, S. G., J. Imberger, and M. L. Morison. 1990. Convective motions in the sidearm of a small reservoir. Limnol. Oceanogr. **35**: 1676–1702. doi:10.4319/lo.1990.35.8.1676

Muster, S., B. Heim, A. Abnizova, and J. Boike. 2013. Water body distributions across scales: A remote sensing based comparison of three arctic tundra wetlands. Remote Sens. **5**: 1498–1523. doi:10.3390/rs5041498

Negandhi, K., I. Laurion, and C. Lovejoy. 2014. Bacterial communities and greenhouse gas emissions of shallow ponds in the high Arctic. Polar Biol. **37**: 1669–1683. doi:10.1007/s00300-014-1555-1

Oakey, N. S. 1982. Determination of the rate of dissipation of turbulent energy from simultaneous temperature and velocity shear microstructure measurements. J. Phys. Oceanogr. **12**: 256–271. doi:10.1175/1520-0485(1982)012<0256:DOTROD>2.0.CO;2

Osborn, T. R. 1980. Estimates of the local-rate of vertical diffusion from dissipation measurements. J. Phys. Oceanogr. **10**: 83–89. doi:10.1175/1520-0485(1980)010<0083:EOTLRO>2.0.CO;2

Read, J. S., and others. 2012. Lake-size dependency of wind shear and convection as controls on gas exchange. Geophys. Res. Lett. **39**. doi:10.1029/2012GL051886

Roiha, T., S. Peura, M. Cusson, and M. Rautio. 2016. Allochthonous carbon is a major regulator to bacterial growth and community composition in subarctic freshwaters. Sci. Rep. **6**: 34456. doi:10.1038/srep34456

Shih, L. H., J. R. Koseff, G. N. Ivey, and J. H. Ferziger. 2005. Parameterization of turbulent fluxes and scales using homogeneous sheared stably stratified turbulence simulations. J. Fluid Mech. **525**: 193–214. doi:10.1017/S0022112004002587

Tedford, E. W., S. MacIntyre, S. D. Miller, and M. J. Czikowsky. 2014. Similarity scaling of turbulence in a small temperate lake during fall cooling. J. Geophys. Res. Oceans **119**: 4689. doi:10.1002/2014JC010135

Tennekes, H., and J. L. Lumley. 1972. A first course in turbulence. MIT Press.

Terray, E., M. Donelan, Y. Agrawal, W. Drennan, K. Kahma, A. Williams, P. Hwang, and S. Kitaigorodskii. 1996. Estimates of kinetic energy dissipation under breaking waves. J. Phys. Oceanogr. **26**: 792–807. doi:10.1175/1520-0485(1996)026<0792:EOKEDU>2.0.CO;2

Thorpe, S. A. 2007. An introduction to ocean turbulence. Cambridge Univ. Press.

Turney, D. E. 2016. Coherent motions and time scales that control heat and mass transfer at wind-swept water surfaces. J. Geophys. Res. Oceans **121**: 8731. doi:10.1002/2016JC012139

Vachon, D., and Y. T. Prairie. 2013. The ecosystem size and shape dependence of gas transfer velocity versus wind speed relationships in lakes. Can. J. Fish. Aquat. Sci. **70**: 1757–1764. doi:10.1139/cjfas-2013-0241

Verpoorter, C., T. Kutser, D. A. Seekell, and L. J. Tranvik. 2014. A global inventory of lakes based on high-resolution satellite imagery. Geophys. Res. Lett. **41**: 6396–6402. doi:10.1002/2014GL060641

Voulgaris, G., and J. H. Trowbridge. 1998. Evaluation of the acoustic Doppler velocimeter (ADV) for turbulence measurements. J. Atmos. Ocean Technol. **15**: 272–289. doi:10.1175/1520-0426(1998)015<0272:EOTADV>2.0.CO;2

Walter Anthony, K., and S. MacIntyre. 2016. Nocturnal escape route for marsh gas. Nature **535**: 363–365. doi:10.1038/535363a

Wang, B., Q. Liao, J. H. Fillingham, and H. A. Bootsma. 2015. On the coefficients of small eddy and surface

divergence models for the air-water gas transfer velocity. J. Geophys. Res. Oceans **120**: 2129–2146. doi:10.1002/2014JC010253

Wang, J., Y. Sheng, K. M. Hinkel, and E. A. Lyons. 2012. Drained thaw lake basin recovery on the western Arctic Coastal Plain of Alaska using high-resolution digital elevation models and remote sensing imagery. Remote Sens. Environ. **119**: 325–336. doi:10.1016/j.rse.2011.10.027

Wik, M., R. K. Varner, K. Walter Anthony, and S. MacIntyre, and D. Bastviken. 2016*a*. High latitude methane release dominated by climate sensitive lake and pond source. Nat. Geosci. **9**: 99–105. doi:10.1038/NGEO2578

Wik, M., B. F. Thornton, D. Bastviken, J. Uhlbäck, and P. M. Crill. 2016*b*. Biased sampling of methane release from northern lakes: A problem for extrapolation. Geophys. Res. Lett. **43**: 1256. doi:10.1002/2015GL066501

Wüest, A., and A. Lorke. 2003. Small-scale hydrodynamics in lakes. Annu. Rev. Fluid Mech. **35**: 373–412. doi:10.1146/annurev.fluid.35.101101.161220

Yvon-Durocher, G., C. J. Hulatt, G. Woodward, and M. Trimmer. 2017. Long-term warming amplifies shifts in the carbon cycle of experimental ponds. Nat. Clim. Change. **7**: 209–213. doi:10.1038/nclimate3229

Zappa, C. J., W. R. McGillis, P. A. Raymond, J. B. Edson, E. J. Hintsa, H. J. Zemmelink, J. W. H. Dacey, and D. T. Ho. 2007. Environmental turbulent mixing controls on air-water gas exchange in marine and aquatic systems. Geophys. Res. Lett. **34**: L10601. doi:10.1029/2006GL028790

Acknowledgments

We thank Erik Young and Jade Lawrence for assistance in the field. We thank Andreas Lorke and an anonymous reviewer for critically reading the manuscript. Meteorological datasets provided by the Toolik Field Station Environmental Data Center are based upon work supported by the U. S. National Science Foundation (NSF) PLR-1623461 and #PLR-1048361. The ARC LTER was funded by NSF DEB-1026843. Logistic support provided by UAF Institute of Arctic Biology (IAB) Toolik Field Station was funded by NSF PLR 1048361. User days at Toolik Field Station were provided by CH2M Polar Services through the NSF's Arctic Research Support and Logistics Program grants #1204267 and #0919603. Funding for L. A. was provided by a VR grant to David Bastviken. This project was supported by NSF Arctic Natural Sciences ARC-120426 and ARC-1737411 to SM.

Conflict of Interest

None declared.

Submitted 15 August 2017
Revised 14 March 2018; 20 April 2018
Accepted 27 April 2018

Associate editor: Craig Stevens